

# Concurrent multi-level model for damage evolution in microstructurally debonding composites

S. Ghosh \*, J. Bai, P. Raghavan

*Department of Mechanical Engineering, The Ohio State University, Columbus, OH 43202, United States*

Received 24 August 2005; received in revised form 4 April 2006

---

## Abstract

This paper develops an adaptive concurrent multi-level computational model for multi-scale analysis of composite structures undergoing damage initiation and growth due to microstructural damage induced by debonding at the fiber–matrix interface. The model combines macroscopic computations using a continuum damage model developed in a preceding paper [Raghavan, P., Ghosh, S., 2005. A continuum damage mechanics model for unidirectional composites undergoing interfacial debonding. *Mech. Mater.* 37 (9), 955–979.] with explicit micromechanical computations of stresses and strain, including explicit debonding at the fiber–matrix interface. The macroscopic computations are done by conventional FEM models while the Voronoi cell FEM is used for micromechanical analysis. Three hierarchical levels of different resolution adaptively evolve in this to improve the accuracy of solutions by reducing modeling and discretization errors. Three levels include: (a) *level-0* of pure macroscopic analysis using a continuum damage mechanics (CDM) model; (b) *level-1* of asymptotic homogenization based macroscopic–microscopic RVE modeling to monitor the breakdown of continuum laws and signal the need for microscopic analyses; and (c) *level-2* regions of pure micromechanical modeling with explicit depiction of the local microstructure. Two numerical examples are solved to demonstrate the effectiveness and accuracy of the multi-scale model. A double lap bonded composite joint is modeled for demonstrating the model’s capability in handling large structural problems.

© 2006 Elsevier Ltd. All rights reserved.

*Keywords:* Composites; Homogenization; Multi-scale modeling; Voronoi cell FEM; Continuum damage mechanics

---

## 1. Introduction

Analysis of composite materials with microstructural heterogeneities is conventionally done with macroscopic properties obtained by homogenizing

response functions in the representative volume element (RVE) from microscopic analyses at smaller length scales. While these “bottom-up” homogenization models are efficient and can reasonably predict macroscopic or averaged behavior, such as stiffness or strength, they have limited predictive capabilities with problems involving localization, failure or instability. Assumptions of macroscopic uniformity and RVE periodicity, the two basic requirements of homogenization, break down under

---

\* Corresponding author. Tel.: +1 614 292 2599; fax: +1 614 292 7369.

E-mail address: [ghosh.5@osu.edu](mailto:ghosh.5@osu.edu) (S. Ghosh).

these circumstances. The uniformity assumption ceases to hold in critical regions of high local solution gradients, such as near free edges, interfaces, material discontinuities or evolving damage. RVE periodicity, on the other hand, is unrealistic for non-uniform microstructures, e.g. in the presence of clustering of heterogeneities or microscopic damage. Even with a uniform phase distribution in the microstructure, the evolution of localized stresses, strains or damage path can violate the periodicity conditions. Problems like this have been effectively tackled by multi-scale modeling methods e.g. in Smit et al. (1998), Fish and Shek (2000), Fish et al. (1999), Oden and Zohdi (1997), Vemaganti and Oden (2001), Ghosh et al. (2001), Raghavan and Ghosh (2004a,b), Terada and Kikuchi (2000), Zohdi and Wriggers (1999) and Tamma and Chung (1999). Multi-scale analyses methods can be broadly classified into two classes. The first is known as “hierarchical models” (Fish and Shek, 2000; Fish et al., 1999; Terada and Kikuchi, 2000; Tamma and Chung, 1999) in which information is passed from lower to higher scales, usually in the form of material properties. The hierarchical homogenization models assume periodic representative volume elements (RVE) in the microstructure and uniformity of macroscopic field variables. The second class, known as “concurrent methods” (Oden and Zohdi, 1997; Vemaganti and Oden, 2001; Ghosh et al., 1995; Raghavan and Ghosh, 2004a,b; Zohdi and Wriggers, 1999), implement sub-structuring and simultaneously solve different models at regions with different resolutions or scales.

The two-way coupling of scales enabled in the concurrent methods is suitable for problems involving localization, damage and failure. Macroscopic analysis, using bottom-up homogenization in regions of relatively benign deformation, enhances the efficiency of the computational analysis. As a matter of fact, it would be impossible to analyze large structural regions without the advantage of a continuum model based macroscopic analysis. On the other hand, the top-down localization process cascading down to the microstructure in critical regions of localized damage or instability for pure microscopic analysis, is necessary for accurately predicting the damage path. These microscopic computations, depicting the real microstructure are often complex and computationally prohibitive. Hence, a concurrent setting makes such analyses feasible, provided the “zoom-in” regions are kept to a minimum. The

adaptive multi-level models, promoted in Oden and Zohdi (1997), Vemaganti and Oden (2001), Ghosh et al. (1995), Raghavan and Ghosh (2004a,b) and Zohdi and Wriggers (1999), are attempts to achieve this objective, with the adaptivity motivated from physical and mathematical perspectives. However, there is a paucity of such studies in the literature involving material nonlinearity and evolving microstructural damage. In their previous studies, Ghosh and coworkers have proposed adaptive multi-level analysis using the microstructural Voronoi cell FEM model for modeling elastic–plastic composites with particle cracking and porosities in Ghosh et al. (2001), and for elastic composites with free edges and stress singularities in Raghavan and Ghosh (2004a,b).

In a preceding paper (Raghavan and Ghosh, 2005), the authors have derived and computationally modeled an anisotropic continuum damage mechanics (CDM) model for unidirectional fiber-reinforced composites undergoing interfacial debonding from by using homogenization theory. The CDM model homogenizes the damage incurred through initiation and growth of interfacial debonding in a microstructural RVE with nonuniform distribution of fibers. Additionally, arbitrary loading conditions are also effectively handled by this model. The present paper uses this CDM model of Raghavan and Ghosh (2005) in an adaptive concurrent multi-level computational model to analyze multi-scale evolution of damage. Damage by fiber–matrix interface debonding, is explicitly modeled over extended microstructural regions at critical locations (Ghosh et al., 2000; Li and Ghosh, 2004). The adaptive model addresses issues of efficiency and accuracy through considerations of physically-based modeling errors.

The adaptive multi-level model consists of three levels of hierarchy viz. *level-0*, *level-1* and *level-2*, which evolve in sequence. The continuum damage model developed in Raghavan and Ghosh (2005) is used for *level-0* computations. The *level-1* domain is used as a ‘swing region’ to establish criteria for switching from macroscopic to microscopic calculations. Physical criteria involving variables at the macroscopic and microstructural RVE levels, trigger switching from pure macroscopic to pure microscopic calculations, i.e. the *level-0* → *level-1* → *level-2*. A transition layer is placed between the *level-1* and microscopic *level-2* domains for smooth transition from one scale to the next. All computations in the composite microstructure with explicit

representations of the fiber and matrix phases are done with the Voronoi cell finite element model or VCFEM (Ghosh et al., 2000; Li and Ghosh, 2004). In VCFEM, debonding at the fiber–matrix interface is achieved by a layer of cohesive springs (Ortiz and Pandolfi, 1999). Two numerical examples are solved in this paper to examine the effectiveness of the multi-level computational model in multi-scale damage analysis. The first example considers a small region of a fiber–matrix composite microstructure for comparison with an explicit micromechanics model. The second set of problems models a double lap bonded composite joint for demonstrating its capability in handling large structural problems.

## 2. Levels in the multi-scale computational model

The multi-phase composite computational domain  $\Omega_{\text{het}}$  is adaptively decomposed into a set of non-intersecting open subdomains, belonging to *levels-0, -1 and -2* with different algorithmic treatments, i.e.  $\Omega_{\text{het}} = \Omega_{l_0} \cup \Omega_{l_1} \cup \Omega_{l_2} \cup \Omega_{\text{tr}}$ . The different levels of computational hierarchy, in the order of sequence of emergence, are depicted in Fig. 1 and discussed briefly here.

### 2.1. Computational subdomain level-0 ( $\Omega_{l_0}$ )

This level corresponds to regions where continuum constitutive laws can be used in macroscopic

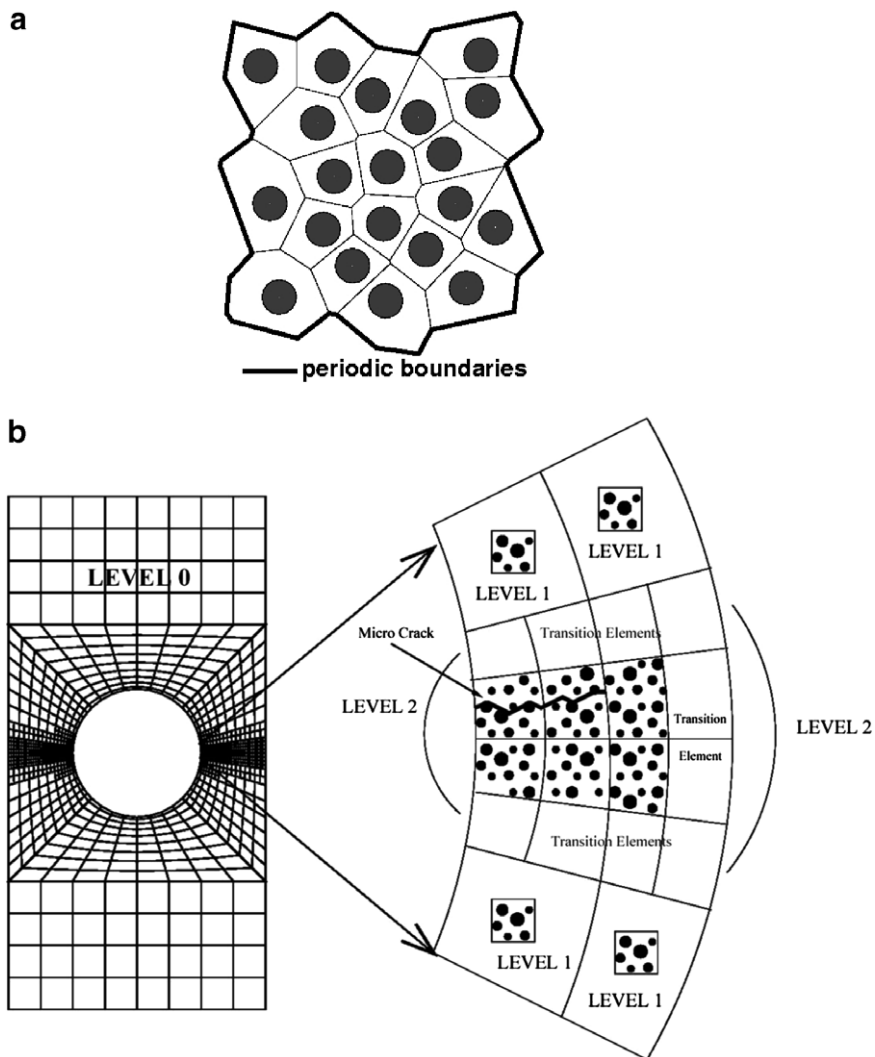


Fig. 1. Schematic of the two-way coupled concurrent multi-level model: (a) a representative volume element (RVE) for a non-uniformly distributed composite microstructure generated by tessellating the local microstructure, (b) the top-down multi-level model showing components of concurrent coupling, viz. continuum *level-0*, *level-1* of asymptotic homogenization and *level-2* of micromechanical analysis.

analysis. Macroscopic field variables like stresses and strains in  $\Omega_0$  are relatively uniform and there is no strong non-periodicity in the microstructure. Hence, microscopic ‘statistical’ periodicity in the RVE is assumed to be valid in this level. Scale effects are negligible and it is possible to derive effective constitutive relations by volume averaging the RVE response with imposed periodicity conditions, in the limit that the RVE tends to zero volume. This is generally the starting level in the multi-scale analysis model, as long as RVE’s can be identified for the computational domain. Macroscopic analysis with the continuum constitutive models in *level-0*, reduce the computing effort by several orders of magnitude in comparison with models that require complete microscopic analysis.

For undamaged microstructures with linear elastic or elastic–plastic phases, homogenized anisotropic constitutive laws have been developed by the authors in Ghosh et al. (1995) and Lee and Ghosh (1999). In the case of microstructures with randomly evolving microcracks causing diffused damage, the homogenized material behavior is best represented by a continuum damage mechanics (CDM) law. An anisotropic CDM model with a fourth order damage tensor has been developed from rigorous micromechanical analyses in Raghavan and Ghosh (2005). The general form of CDM models (Kachanov, 1987) introduce a fictitious effective stress  $\tilde{\Sigma}_{ij}$  acting on an effective resisting area ( $\tilde{A}$ ), which is caused by reduction of the original resisting area  $A$  due to material degradation from the presence of microcracks and stress concentration in the vicinity of cracks. In Raghavan and Ghosh (2005), the effective stress  $\tilde{\Sigma}_{ij}$  is related to the actual Cauchy stress  $\Sigma_{ij}$  through the fourth order damage effect tensor  $M_{ijkl}$  as

$$\tilde{\Sigma}_{ij} = M_{ijkl}(\mathbf{D})\Sigma_{kl} \quad (1)$$

where  $M_{ijkl}$  is a function of the fourth order damage tensor  $\mathbf{D}$  ( $=D_{ijkl}\mathbf{e}_i \otimes \mathbf{e}_j \otimes \mathbf{e}_k \otimes \mathbf{e}_l$ ). The hypothesis of equivalent elastic energy is used to evaluate  $M_{ijkl}$  and hence establish a relation between the damaged and undamaged stiffnesses (Cordebois and Sidoroff, 1982; Chow and Wang, 1987; Zhu and Cescotto, 1995). Equivalence is established by equating the elastic energy in the damaged state to that in a hypothetical undamaged state as

$$\begin{aligned} W(\Sigma, \mathbf{D}) &= \frac{1}{2}\Sigma_{ij}(E_{ijkl}(\mathbf{D}))^{-1}\Sigma_{kl} = W(\tilde{\Sigma}, \mathbf{0}) \\ &= \frac{1}{2}\tilde{\Sigma}_{ij}(E_{ijkl}^0)^{-1}\tilde{\Sigma}_{kl} \end{aligned} \quad (2)$$

where  $\Sigma = \Sigma_{ij}\mathbf{e}_i \otimes \mathbf{e}_j$ ,  $E_{ijkl}^0$  is the elastic stiffness tensor in the undamaged state and  $E_{ijkl}(\mathbf{D})$  is the stiffness in a damaged state. From Eqs. (1) and (2), the relation between the damaged and undamaged stiffnesses is established as

$$E_{ijkl} = (M_{pqij})^{-1}E_{pqrs}^0(M_{rskl})^{-1} \quad (3)$$

With an appropriate assumption of a function for  $M_{ijkl}$ , Eq. (3) can be used to formulate a damage evolution model using micromechanics and homogenization. In Raghavan and Ghosh (2005), a damage evolution surface is introduced to delineate the interface between damaged and undamaged domains in the strain  $\mathbf{e}$ -space as

$$F = \frac{1}{2}e_{ij}P_{ijkl}e_{kl} - \kappa(\alpha W_d) = 0 \quad (4)$$

Here  $W_d$  corresponds to the dissipation of the strain energy density due to stiffness degradation for constant strain without an external work supply. Also called the degrading dissipation energy (see Carol et al., 1994), it is an internal variable denoting the current state of damage, and is expressed as

$$W_d = \int \frac{1}{2}e_{ij}e_{kl} dE_{ijkl} \quad (5)$$

$P_{ijkl}$  is a symmetric negative-definite fourth order tensor that will be expressed as a function of the strain tensor  $e_{ij}$ ,  $\alpha$  is a scaling parameter and  $\kappa$  is a function of  $W_d$ . Assuming associativity rule in the stiffness space, the evolution of the fourth order secant stiffness is obtained as

$$\dot{E}_{ijkl} = \dot{\lambda} \frac{\partial F}{\partial (\frac{1}{2}e_{ij}e_{kl})} = \dot{\lambda} P_{ijkl} \quad (6)$$

$P_{ijkl}(\mathbf{e})$  corresponds to the direction of the rate of stiffness degradation tensor  $\dot{E}_{ijkl}$ . For a composite material with interfacial debonding, the direction of rate of stiffness degradation varies with increasing damage and hence  $P_{ijkl}(\mathbf{e})$  does not remain a constant throughout the loading process. The model requires the evaluation of  $\kappa$ ,  $\alpha$  and  $P_{ijkl}$  in Eq. (4). These are determined from the results of micromechanical simulations of a RVE with periodic boundary conditions. The function  $\kappa(W_d)$  is evaluated for a reference loading path and all other strain paths are scaled with respect to this reference. Upon determination of the maximum value  $W_d$  for a reference loading condition, the value of  $\alpha$  for any strain path can be obtained by simple scaling. To account for the variation of  $P_{ijkl}(\mathbf{e})$ , any macroscopic strain evolution path is discretized into a finite set of points.

The values of  $P_{ijkl}$  are explicitly evaluated at these points from RVE based simulations. Values of  $P_{ijkl}$  for any arbitrary macroscopic strain value can then be determined by interpolating between nodal values using shape functions of a 3D linear hexahedral element. The details of the parameter evaluation process in the macroscopic CDM model are discussed in Raghavan and Ghosh (2005).

2.2. Computational subdomain level-1 ( $\Omega_{II}$ )

Level-1 is an intermediate computational subdomain, introduced as a swing region for establishing criteria for switching from macroscopic level-0 regions to level-2 regions of pure microscopic computations. The switching criteria are based on analyses of the macroscopic problem, as well as of the microstructural RVE problem. The asymptotic homogenization theory is used for this level to decouple the set of governing equations into a set of (i) homogenized equations representing the macroscopic problem corresponding to a length scale  $\mathbf{x}$  and (ii) microscopic equations for the RVE  $Y(\mathbf{x})$ , represented by a length scale  $\mathbf{y}$ . Any function  $f$  in the RVE is assumed to be  $Y$ -periodic, i.e.  $f(\mathbf{x}, \mathbf{y}) = f(\mathbf{x}, \mathbf{y} + \mathbf{kY}) \forall k = 1, 2, \dots$ . Periodicity conditions are used on the RVE boundary to decouple the set of equations at different levels as

Microscopic equations

$$\begin{aligned} \epsilon_{ij}(\mathbf{x}, \mathbf{y}) &= e_{ij}(\mathbf{x}) + \frac{1}{2} \left( \frac{\partial u_i(\mathbf{y})}{\partial y_j} + \frac{\partial u_j(\mathbf{y})}{\partial y_i} \right) \\ &= e_{kl}(\mathbf{x}) \left[ \delta_{ki} \delta_{lj} + e_{ki}^{-1}(\mathbf{x}) \frac{\partial u_l(\mathbf{y})}{\partial y_j} \right] \quad (\text{Kinematics}) \\ \sigma_{ij}(\mathbf{x}, \mathbf{y}) &= E_{ijkl} \left[ \delta_{mk} \delta_{nl} + e_{mk}^{-1}(\mathbf{x}) \frac{\partial u_n(\mathbf{y})}{\partial y_l} \right] e_{mn}(\mathbf{x}) \quad (\text{Constitutive}) \\ \frac{\partial \sigma_{ij}(\mathbf{x}, \mathbf{y})}{\partial y_j} &= 0 \quad (\text{Equilibrium}) \end{aligned} \tag{7}$$

Macroscopic equations

$$\begin{aligned} \Sigma_{ij}(\mathbf{x}) &= \frac{1}{|Y|} \int_Y E_{ijkl} \left( \delta_{km} \delta_{ln} + e_{km}^{-1} \frac{\partial u_n}{\partial y_l} \right) dY e_{mn} \\ &= E_{ijmn}^H e_{mn}(\mathbf{x}) \quad (\text{Constitutive}) \\ \frac{\partial \Sigma_{ij}(\mathbf{x})}{\partial x_j} + f_i &= 0 \quad (\text{Equilibrium}) \end{aligned} \tag{8}$$

In the above equations  $u_i$  is a  $Y$ -periodic displacement function and  $\sigma_{ij}(\mathbf{x}, \mathbf{y})$  is the stress field in the RVE respectively, while  $\Sigma_{ij}(\mathbf{x})$  and  $e_{ij}$  are the homogenized stress and strain tensors.  $E_{ijkl}$  and

$E_{ijkl}^H$  correspond to microscopic and homogenized anisotropic elasticity tensor respectively. The details of the derivation of Eqs. (7) and (8) are discussed in Ghosh et al. (2001) and Raghavan and Ghosh (2004a).

Gradients of important field variables are evaluated from macroscopic analysis to assess the deviation of macroscopic uniformity. Such gradients may be the effect of strong microscopic non-homogeneity in the form of highly localized stresses and strains or damage. The RVE-based microscopic analysis, on the other hand, provides effective criteria to estimate departure from periodicity conditions, especially in the event of evolving microstructural damage. The adaptation criteria for level transitions are discussed in Section 4. Two sets of finite element problems are solved for the level-1 subdomain in sequence, viz.,

- (1) *Macroscopic analysis:* Incremental macroscopic analysis of the computational domain is performed using the CDM model to evaluate macroscopic variables e.g. stresses and strains due to the increments in applied loads.
- (2) *Microstructural RVE analysis:* This is a post-processing operation in which microstructural analysis of the RVE is conducted for each integration point of the macroscopic elements. The strain field  $e_{ij}$ , obtained from macroscopic analysis with the CDM model, is imposed on the RVE as an external driver, together with periodic boundary conditions on the boundary of the RVE as shown in Fig. 1a. Microscopic stresses  $\sigma_{ij}$ , strains  $\epsilon_{ij}$  and other variables are computed in this post-processing stage for each RVE.

**Remark 1.** The macroscopic computations of level-0 and level-1 elements are performed with the conventional displacement-based finite element method, while all microscopic calculations in the RVE of level-1 elements are performed using the Voronoi cell FEM (Moorthy and Ghosh, 2000; Ghosh et al., 2000; Li and Ghosh, 2004).

**Remark 2.** Computational models in the macroscopic level-0 and level-1 subdomains are refined adaptively by selective  $h$ - or  $h$ - $p$  strategies. ‘Error’ and convergence criteria for this refinement have been discussed in Raghavan and Ghosh (2004a). Local enrichment through successive mesh refinement or enhancement, serves a dual purpose in the multi-level computational strategy. The first goal

is to identify regions of high discretization ‘error’ and improve convergence through mesh enhancement. The second is to identify regions of high modeling error and zoom in on these regions to create higher resolution. These regions are generally characterized by large gradients and localization of macroscopic variables. Element refinement in these regions is helpful for reducing the length-scale difference between macroscopic elements in the homogenized domain and microscopic regions with explicit representation of heterogeneities.

2.3. Computational subdomain level-2 ( $\Omega_{l2}$ )

The *level-2* subdomain of pure microscopic analysis emerges from *level-1* elements in regions characterized by (a) departure from macroscopic uniformity, e.g. regions of localization or fracture, and (b) significant microstructural non-uniformities manifested by e.g. growth of localized damage. Prior to transition to *level-2* elements, a high spatial resolution is reached in the macroscopic mesh, resulting in small elements, by *h*- or *hp*-refinement. The successive refinement process stops when a certain element size is achieved and subsequently the model changes from macroscopic to pure microscopic. A scale ratio *SR* is chosen a priori to ascertain this element size. Depending on the choice of  $SR = \frac{\text{Size of level-2 element}}{\text{Size of local RVE}}$ , the microscopic model in any given *level-2* element can encompass large portions of the microstructure with many discrete heterogeneities. The *level-2* elements are constructed by filling with the exact microstructure at that location, as outlined in the following steps and shown in Fig. 2:

- Use appropriate adaptation criteria to determine if a *level-1* element needs to switch to *level-2* element.
- Identify a region in the microstructure  $\Omega_{\text{micro}}$  that is located in the same region as the *level-2* element.  $\Omega_{\text{micro}}$  should extend beyond the element boundary by approximately two fiber lengths.
- Tessellate the local microstructure to generate a mesh of Voronoi cell elements as shown in Fig. 3.
- Carve out the microstructural region of the *level-2* element from the local microstructure  $\Omega_{\text{micro}}$ . This procedure will result in dissecting some of the fibers on the boundary. When this happens, additional nodes are generated on the Voronoi cell boundary at locations where the fiber surface

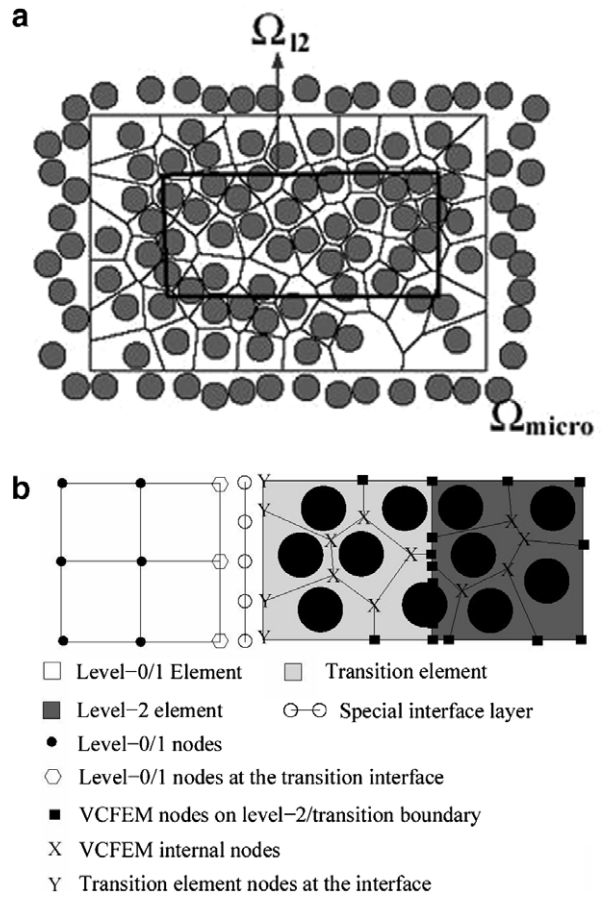


Fig. 2. (a) Process of carving out *level-2* element microstructure (b) Interface constraints between *level-0/level-1* and tr elements.

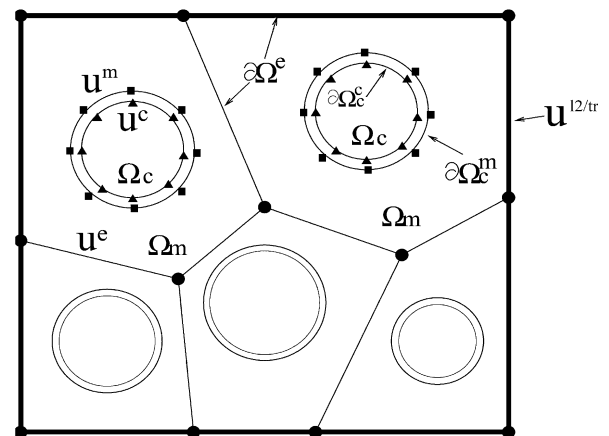


Fig. 3. A typical *level-2* element containing an aggregate of microstructural Voronoi cell elements with relevant notations.

and Voronoi cell edges intersect the boundary of the *level-2* element. The dissected conjugate

pieces of a fiber belonging to two contiguous *level-2* elements are joined together when the two contiguous elements share a common edge.

Requirement of high-resolution micromechanical models in these elements entails prohibitively large computations using conventional finite element methods. The microstructure-based Voronoi cell FEM (Ghosh et al., 2000; Li and Ghosh, 2004; Moorthy and Ghosh, 2000) is particularly effective for modeling *level-2* elements because of its efficiency in modeling large heterogeneous regions (Ghosh et al., 2000; Li and Ghosh, 2004; Moorthy and Ghosh, 2000; Ghosh and Moorthy, 1998; Ghosh et al., 2001; Raghavan and Ghosh, 2004a). Each Voronoi cell with embedded heterogeneities (particle, fiber, void, crack etc.) represents the region of contiguity for the heterogeneity, and is treated as an element in VCFEM. VCFEM elements can be considerably larger than conventional FEM elements and incorporate a special hybrid FEM formulation. Incorporation of known functional forms from analytical micromechanics substantially enhances its convergence. A schematic diagram of Voronoi cell elements is shown in Fig. 3. A high level of accuracy has been achieved with VCFEM for modeling problems with microstructural damage by particle cracking (Ghosh and Moorthy, 1998) and fiber–matrix interfacial debonding (Ghosh et al., 2000; Li and Ghosh, 2004). For debonding simulation, imperfect interfaces are represented by the cohesive zone model (Ortiz and Pandolfi, 1999). Displacement degrees of freedom on the fiber–matrix interface are constrained by the cohesive zone models as discussed in Section 3. VCFEM has been shown to be significantly more efficient than commercial displacement based FE packages for modeling complex microstructures with evolving damage.

#### 2.4. Scale transition subdomain ( $\Omega_{tr}$ )

The interface between the *level-0* or *level-1* elements and the *level-2* elements with explicit representation of the heterogeneous microscopic domain, needs a special treatment to facilitate smooth transition of scales across the element boundaries. A layer of transition elements ( $E_{tr} \in \Omega_{tr}$ ) is sandwiched between these elements, where ( $\Omega_{tr}$ ) is the transition subdomain as shown in Fig. 2b. The  $E_{tr}$  elements are essentially *level-2* elements with compatibility and traction continuity constraints imposed at the interface with *level-0/level-1* elements. It is assumed

that layers of  $E_{tr}$  elements are located beyond the critical hot-spots, at which homogenization fails. Hence, the homogenized laws are sufficient at their interfaces with *level-1/level-0* elements. A weak form of the interface displacement continuity is incorporated through the use of Lagrange multipliers on this interface (Raghavan and Ghosh, 2004a,b). This results in a weak satisfaction of the interface displacement compatibility and avoids the occurrence of spurious forces that arise if the displacements are strongly coupled.

### 3. Coupling different levels in the concurrent multi-scale algorithm

The concurrent multi-scale analysis requires that all levels be coupled for simultaneously solving for variables in the different computational subdomains. Consequently, the global stiffness matrix and load vectors are derived for the entire computational domain ( $\Omega_{het} = \{\Omega_{10} \cup \Omega_{11} \cup \Omega_{12} \cup \Omega_{tr}\}$ ). The corresponding domain boundary is delineated as  $\Gamma_{het} = \{\Gamma_{10} \cup \Gamma_{11} \cup \Gamma_{12}\}$  where  $\Gamma_{10} = \partial\Omega_{10} \cap \Gamma_{het}$ ;  $\Gamma_{11} = \partial\Omega_{11} \cap \Gamma_{het}$ ;  $\Gamma_{12} = \partial\Omega_{12} \cap \Gamma_{het}$ . Let  $\Gamma_{int} = \partial\Omega_{11} \cap \partial\Omega_{tr}$  delineate the boundary between the *level-1* and transition elements, where the displacement continuity is satisfied using Lagrange multipliers. The incremental form of the equation of principle of virtual work equation for  $\Omega_{het}$  at the end of an increment, can be written as the sum of contributions from each individual domain, as

$$\begin{aligned} & \int_{\Omega_{10}} (\Sigma_{ij} + \Delta\Sigma_{ij}) \frac{\partial \delta u_i^{10}}{\partial x_j} d\Omega - \int_{\Gamma_{10}} (t_i + \Delta t_i) \delta u_i^{10} d\Gamma \\ & + \int_{\Omega_{11}} (\Sigma_{ij} + \Delta\Sigma_{ij}) \frac{\partial \delta u_i^{11}}{\partial x_j} d\Omega - \int_{\Gamma_{11}} (t_i + \Delta t_i) \delta u_i^{11} d\Gamma \\ & + \int_{\Omega_{tr}} (\sigma_{ij} + \Delta\sigma_{ij}) \frac{\partial \delta u_i^{tr}}{\partial x_j} d\Omega - \int_{\Gamma_{tr}} (t_i + \Delta t_i) \delta u_i^{tr} d\Gamma \\ & + \int_{\Omega_{12}} (\sigma_{ij} + \Delta\sigma_{ij}) \frac{\partial \delta u_i^{12}}{\partial x_j} d\Omega - \int_{\Gamma_{12}} (t_i + \Delta t_i) \delta u_i^{12} d\Gamma \\ & + \delta \int_{\Gamma_{int}} (\lambda_i^{10/11} + \Delta\lambda_i^{10/11})(v_i + \Delta v_i - u_i^{10/11} - \Delta u_i^{10/11}) d\Gamma \\ & + \delta \int_{\Gamma_{int}} (\lambda_i^{tr} + \Delta\lambda_i^{tr})(v_i + \Delta v_i - u_i^{tr} - \Delta u_i^{tr}) d\Gamma = 0 \end{aligned} \tag{9}$$

The prefix  $\Delta$  symbolizes increments of the respective variables in the incremental solution process. The superscripts 10, 11, 12, tr correspond to association with the respective level, while the (/) sign refers to

variables that could belong to either level.  $\Sigma_{ij}$  are the components homogenized macroscopic stresses obtained from the CDM constitutive model for  $\Omega_{10}$  and  $\Omega_{11}$ . The applied tractions  $t_i$  are at traction boundaries of the respective domains. The boxed parts in Eq. (9) correspond to contributions from *level-2* and transition computational subdomains that are generated from VCFEM solutions of the microstructural regions. Displacement components  $u_i^{10}$ ,  $u_i^{11}$ ,  $u_i^{\text{tr}}$  and  $u_i^{12}$  are on the boundaries of elements coinciding with the boundaries of the  $\Omega_{10}$ ,  $\Omega_{11}$ ,  $\Omega_{\text{tr}}$  and  $\Omega_{12}$  subdomains. An intermediate segment  $\Gamma_{\text{int}}$  is added at the interface between the *level-1* and *tr* elements, as shown in Fig. 2b. On these segments, displacement components  $v_i$  are interpolated with any order polynomial functions, independent of the interpolations on  $\partial\Omega^{10/11}$  or  $\partial\Omega^{\text{tr}}$ . Even for highly nonhomogeneous displacements, high order interpolations on the intermediate segment are able to smoothen the transition between levels. This has been demonstrated for problems without damage through numerical examples in Raghavan and Ghosh (2004a). The last two terms in Eq. (9) use Lagrange multipliers to facilitate incorporation of a weak form of the interfacial displacement continuity on  $\Gamma_{\text{int}}$ .  $\lambda^{10/11}$  and  $\lambda^{\text{tr}}$  are vector columns of Lagrange multipliers belonging to domains  $\Omega_{10/11}$  and  $\Omega_{\text{tr}}$  respectively at  $\Gamma_{\text{int}}$ . The Euler's equations, obtained from setting the coefficients of  $\delta v_i$ ,  $\delta\lambda_i^{10/11}$  and  $\delta\lambda_i^{\text{tr}}$  to zero respectively in the principle of virtual work (9), are

$$\begin{aligned} \lambda_i^{10/11} + \Delta\lambda_i^{10/11} &= (\sigma_{ij} + \Delta\sigma_{ij})^{10/11} n_j = -(\lambda_i^{\text{tr}} + \Delta\lambda_i^{\text{tr}}) \\ &= -(\sigma_{ij} + \Delta\sigma_{ij})^{\text{tr}} n_j \\ (u_i + \Delta u_i)^{10/11} &= (u_i + \Delta u_i)^{\text{tr}} = (v_i + \Delta v_i) \end{aligned} \tag{10}$$

where  $n_i$  is the unit normal vector and  $\lambda_i^{10/11}$  and  $\lambda_i^{\text{tr}}$  correspond to the interfacial traction components on  $\partial\Omega_{10/11}$  and  $\partial\Omega_{\text{tr}}$  respectively. The displacements  $v_i$  and the Lagrange multipliers  $\lambda_i^{10/11}$  and  $\lambda_i^{12/\text{tr}}$  on the intermediate boundary segment are interpolated from nodal values using suitably assumed shape functions as

$$\begin{aligned} \{\mathbf{v}\} &= [L_{\text{int}}]\{\mathbf{q}_{\text{int}}\}, \\ \{\lambda^{10/11}\} &= [L_{\lambda^{10/11}}]\{\Lambda_{10/11}\}, \quad \{\lambda^{\text{tr}}\} = [L_{\lambda^{\text{tr}}}] \{\Lambda_{\text{tr}}\} \end{aligned} \tag{11}$$

The displacements  $u_i^{10}$  and  $u_i^{11}$  in each *level-0* and *level-1* elements are interpolated by the standard or hierarchical Legendre polynomials based shape functions as

$$\begin{aligned} \{\mathbf{u}\}^{10} &= [\mathbf{N}_{10}]\{\mathbf{q}_{10}\} = [\mathbf{N}_{10}^{\text{I}}\mathbf{N}_{10}^{\text{O}}] \begin{Bmatrix} \mathbf{q}_{10}^{\text{I}} \\ \mathbf{q}_{10}^{\text{O}} \end{Bmatrix} \\ \{\mathbf{u}\}^{11} &= [\mathbf{N}_{11}]\{\mathbf{q}_{11}\} = [\mathbf{N}_{11}^{\text{I}}\mathbf{N}_{11}^{\text{O}}] \begin{Bmatrix} \mathbf{q}_{11}^{\text{I}} \\ \mathbf{q}_{11}^{\text{O}} \end{Bmatrix} \end{aligned} \tag{12}$$

As shown in Fig. 2b, the generalized displacements in the *level-0* and *level-1* elements are subdivided into two classes: (i) those at nodal points, which interface with transition elements, and (ii) those at all other nodes. Generally, only *level-1* elements will interface with transition elements because of the sequence of introduction of computational levels. The generalized displacements  $\mathbf{q}_{10/11}^{\text{I}}$  corresponds to the nodal degrees of freedom in *level-0/level-1* elements at the interface with transition elements, while  $\mathbf{q}_{10/11}^{\text{O}}$  correspond to the remaining degrees of freedom in these elements. The solution of the algebraic form of Eq. (9) is obtained using the Newton–Raphson iterative solver. Setting up the tangent stiffness matrix requires consistent linearization by taking directional derivative of Eq. (9) along incremental displacement vectors  $\Delta\mathbf{u}$  and  $\Delta\mathbf{v}$ , and the Lagrange multipliers  $\Delta\lambda$ . For the  $i$ th iteration in the solution of the incremental variables, assembled matrix equations derived from Eq. (9) has the following structure:

$$\begin{bmatrix} \mathbf{K}_{10/11}^{\text{I,I}} & \mathbf{K}_{10/11}^{\text{I,O}} & 0 & 0 & 0 & \mathbf{P}_{10/11} & 0 \\ \mathbf{K}_{10/11}^{\text{O,I}} & \mathbf{K}_{10/11}^{\text{O,O}} & 0 & 0 & 0 & 0 & 0 \\ 0 & 0 & \mathbf{K}_{\text{tr}}^{\text{I,I}} & \mathbf{K}_{\text{tr}}^{\text{I,O}} & 0 & 0 & \mathbf{P}_{\text{tr}} \\ 0 & 0 & \mathbf{K}_{\text{tr}}^{\text{O,I}} & \mathbf{K}_{12/\text{tr}}^{\text{O,O}} & 0 & 0 & 0 \\ 0 & 0 & 0 & 0 & 0 & \mathbf{Q}_{10/11} & \mathbf{Q}_{\text{tr}} \\ \mathbf{P}_{10/11}^{\text{T}} & 0 & 0 & 0 & \mathbf{Q}_{10/11}^{\text{T}} & 0 & 0 \\ 0 & 0 & \mathbf{P}_{\text{tr}}^{\text{T}} & 0 & \mathbf{Q}_{\text{tr}}^{\text{T}} & 0 & 0 \end{bmatrix}^i \times \begin{Bmatrix} \Delta\mathbf{q}_{10/11}^{\text{I}} \\ \Delta\mathbf{q}_{10/11}^{\text{O}} \\ \Delta\mathbf{q}_{\text{tr}}^{\text{I}} \\ \Delta\mathbf{q}_{12/\text{tr}}^{\text{O}} \\ \Delta\mathbf{q}_{\text{int}} \\ \Delta\Lambda_{10/11} \\ \Delta\Lambda_{\text{tr}} \end{Bmatrix}^i = \begin{Bmatrix} \Delta\mathbf{F}_{10/11}^{\text{I}} \\ \Delta\mathbf{F}_{10/11}^{\text{O}} \\ \Delta\mathbf{F}_{\text{tr}}^{\text{I}} \\ \Delta\mathbf{F}_{12/\text{tr}}^{\text{O}} \\ \Delta\mathbf{F}_{\text{int}} \\ \Delta\mathbf{F}_{\lambda^{10/11}} \\ \Delta\mathbf{F}_{\lambda^{12/\text{tr}}} \end{Bmatrix}^i \tag{13}$$

As explained before, the superscript I represents quantities associated with nodal points at the interface with transition elements while superscript O indicate association with nodes at other regions. The two notations in the superscript separated by comma, represents the node coupling effect. For example, the superscript I, O corresponds to the

coupling between the non-interface and interface nodes. The stiffness submatrices  $[\mathbf{K}_{10/11}]$  and sub-vector  $\{\mathbf{F}_{10/11}\}$  correspond to those for the *level-0* and *level-1* elements and are expressed as

$$\begin{aligned} (K_{10/11})_{mzn\beta} &= \int_{\Omega_{10} \cup \Omega_{11}} \frac{\partial N_\alpha}{\partial x_k} \frac{\partial \Sigma_{mn}}{\partial e_{kl}} \frac{\partial N_\beta}{\partial x_l} d\Omega \\ (\Delta \mathbf{F}_{10/11})_{mz} &= \int_{\Gamma_i} (t_m + \Delta t_m) N_\alpha d\Gamma + \int_{\Gamma_{\text{int}}} (\lambda_m + \Delta \lambda_m) N_\alpha d\Gamma \\ &\quad - \int_{\Omega_{10} \cup \Omega_{11}} (\Sigma_{mn} + \Delta \Sigma_{mn}) \frac{\partial N_\alpha}{\partial x_n} d\Omega \end{aligned} \quad (14)$$

The subscripts  $(m, n)$  correspond to the degrees of freedom while  $(\alpha, \beta)$  correspond to the node numbers in the element. These matrices and vectors are further divided based on the classification of the I and O nodes. The coupling between the *level-0/level-1* and tr elements is achieved through the  $[\mathbf{P}]$  and  $[\mathbf{Q}]$  matrices, which may be expressed as

$$\begin{aligned} (P_{10/11})_{mzn\beta} &= - \int_{\Gamma_{\text{int}}} \mathbf{N}_{mz}^T (\mathbf{L}_{\lambda^{10/11}})_{n\beta} d\Gamma \\ (P_{\text{tr}})_{mzn\beta} &= - \int_{\Gamma_{\text{int}}} \mathbf{N}_{mz}^T (\mathbf{L}_{\lambda^{12/\text{tr}}})_{n\beta} d\Gamma \\ (Q_{10/11})_{mzn\beta} &= \int_{\Gamma_{\text{int}}} (\mathbf{L}_{\text{int}}^T)_{mz} (\mathbf{L}_{\lambda^{10/11}})_{n\beta} d\Gamma \\ (Q_{\text{tr}})_{mzn\beta} &= \int_{\Gamma_{\text{int}}} (\mathbf{L}_{\text{int}}^T)_{mz} (\mathbf{L}_{\lambda^{\text{tr}}})_{n\beta} d\Gamma \end{aligned} \quad (15)$$

Contributions to the load vector  $\{\mathbf{F}\}$  due to coupling between *level-0/level-1* and tr elements are given as

$$\begin{aligned} (\Delta F_{\text{int}})_{mz} &= - \int_{\Gamma_{\text{int}}} (L_{\text{int}}^T)_z (\lambda^{10/11} + \Delta \lambda^{10/11})_m d\Gamma \\ &\quad - \int_{\Gamma_{\text{int}}} (L_{\text{int}}^T)_z (\lambda^{12/\text{tr}} + \Delta \lambda^{12/\text{tr}})_m d\Gamma \\ (\Delta F_{\lambda^{10/11}})_{mz} &= - \int_{\Gamma_{\text{int}}} (L_{\lambda^{10/11}}^T)_z \{v_m + \Delta v_m - (u_{10/11})_m - \Delta (u_{10/11})_m\} d\Gamma \\ (\Delta F_{\lambda^{12/\text{tr}}})_{mz} &= - \int_{\Gamma_{\text{int}}} (L_{\lambda^{\text{tr}}}^T)_z \{v_m + \Delta v_m - (u_{12/\text{tr}})_m - \Delta (u_{12/\text{tr}})_m\} d\Gamma \end{aligned} \quad (16)$$

Finally, the stiffness  $[\mathbf{K}_{12/\text{tr}}]$  and the load vector  $\{\mathbf{F}_{12/\text{tr}}\}$  for *level-2* and tr elements are obtained by VCFEM calculations followed by static condensation to represent the virtual work in terms of the boundary terms only.

### 3.1. The voronoi cell finite element model

Details of the Voronoi Cell FEM are provided in Moorthy and Ghosh (2000), Ghosh et al. (2000) and Li and Ghosh (2004) and will only be summarized here. A typical *level-2/transition* element consisting of microstructural Voronoi cell elements is shown in Fig. 3. The following assumptions are made in the formulation of each VCFEM element:

- Stress fields  $\sigma_{ij}^m$  in the matrix phase  $\Omega_m$  and  $\sigma_{ij}^c$  in the inclusion phase  $\Omega_c$  of each Voronoi cell element  $\Omega_e$  are independent and equilibrated. The stress interpolations in each phase are expressed as  $\{\boldsymbol{\sigma}^m\} = [\mathbf{P}^m]\{\boldsymbol{\beta}^m\}$  in  $\Omega_m$  and  $\{\boldsymbol{\sigma}^c\} = [\mathbf{P}^c]\{\boldsymbol{\beta}^c\}$  in  $\Omega_c$  (17) where the matrices  $[\mathbf{P}^{m/c}]$  are obtained from assumed stress functions like the Airy's stress function and  $\{\boldsymbol{\beta}^{m/c}\}$  are unknown coefficients to be solved.
- Compatible displacement field  $u_i^e$  are assumed on each Voronoi cell element boundary  $\partial\Omega_e$  and interpolated as  $\{\mathbf{u}^e\} = [\mathbf{L}^e]\{\mathbf{q}^e\}$  (18)
- Compatible displacement fields  $u_i^m$  and  $u_i^c$  are assumed on the matrix and inclusion sides of the matrix–inclusion interface  $\partial\Omega_c$  respectively, and are interpolated as  $\{\mathbf{u}^m\} = [\mathbf{L}^c]\{\mathbf{q}^m\}$  on  $\partial\Omega_c^m$  and  $\{\mathbf{u}^c\} = [\mathbf{L}^c]\{\mathbf{q}^c\}$  on  $\partial\Omega_c^c$  (19)

In an incremental formulation, the potential energy functional for each element is expressed in terms of the incremented stresses and displacements as

$$\begin{aligned} \Pi_e(\sigma_{ij}^m, \Delta \sigma_{ij}^m, \sigma_{ij}^c, \Delta \sigma_{ij}^c, u_i^e, \Delta u_i^e, u_i^m, \Delta u_i^m, u_i^c, \Delta u_i^c) &= - \int_{\Omega_m} \Delta B^m(\sigma_{ij}^m, \Delta \sigma_{ij}^m) d\Omega - \int_{\Omega_c} \Delta B^c(\sigma_{ij}^c, \Delta \sigma_{ij}^c) d\Omega \\ &\quad + \int_{\Omega_m} (\sigma_{ij}^m + \Delta \sigma_{ij}^m)(\epsilon_{ij}^m + \Delta \epsilon_{ij}^m) d\Omega \\ &\quad + \int_{\Omega_c} (\sigma_{ij}^c + \Delta \sigma_{ij}^c)(\epsilon_{ij}^c + \Delta \epsilon_{ij}^c) d\Omega \\ &\quad - \int_{\partial\Omega_c} \int_{u_n^m - u_n^c}^{u_n^m + \Delta u_n^m - u_n^c - \Delta u_n^c} T_n^m d(u_n^m - u_n^c) d\partial\Omega \\ &\quad - \int_{\partial\Omega_c} \int_{u_t^m - u_t^c}^{u_t^m + \Delta u_t^m - u_t^c - \Delta u_t^c} T_t^m d(u_t^m - u_t^c) d\partial\Omega \\ &\quad - \int_{\Gamma_m} (t_i + \Delta t_i)(u_i^e + \Delta u_i^e) d\Gamma \end{aligned} \quad (20)$$

Here  $B = \frac{1}{2}S_{ijkl}\sigma_{ij}\sigma_{kl}$  is the complementary energy density and  $\Delta B = \frac{1}{2}S_{ijkl}\Delta\sigma_{ij}\Delta\sigma_{kl} + S_{ijkl}\Delta\sigma_{ij}\sigma_{kl}$ . The strain fields  $\epsilon_{ij}^m$  and  $\epsilon_{ij}^c$  are in the matrix and inclusion phases respectively of each Voronoi element.  $\mathbf{t}$  is the prescribed traction on the boundary  $\Gamma_{tm}$ . The prefix  $\Delta$  corresponds to increments and subscripts n and t correspond to the normal and tangential directions at the matrix–inclusion interface. The two terms on the matrix–inclusion interface  $\partial\Omega^m/\partial\Omega^c$  provide the work done by the interfacial tractions  $\mathbf{T}^m = T_n^m\mathbf{n}^m + T_t^m\mathbf{t}^m$  due to interfacial separation  $(\mathbf{u}^m - \mathbf{u}^c)$ .  $T_n^m$  and  $T_t^m$  are the normal and tangential components that are described by cohesive laws in Ghosh

tal displacements at the interface  $\partial\Omega_c$  is conducted by the backward Euler method. The total potential energy functional for each level-2 or tr element containing  $N_{vc}$  Voronoi cell elements as shown in Fig. 3 is

$$\Pi^{l2/tr} = \sum_{e=1}^{N_{vc}} \Pi_e \tag{22}$$

Substituting stress interpolations (17) and displacement interpolations (18), (19) in Eq. (21) and setting variations with respect to the stress coefficients  $\Delta\boldsymbol{\beta}^m$ ,  $\Delta\boldsymbol{\beta}^c$  respectively to zero results in the weak form of the element kinematic relation

$$\begin{aligned} & \left[ \begin{array}{cc} \int_{\Omega_m} [\mathbf{P}^m]^T [\mathbf{S}^m] [\mathbf{P}^m] d\Omega & [\mathbf{0}] \\ [\mathbf{0}] & \int_{\Omega_c} [\mathbf{P}^c]^T [\mathbf{S}^c] [\mathbf{P}^c] d\Omega \end{array} \right] \left\{ \begin{array}{l} \boldsymbol{\beta}^m + \Delta\boldsymbol{\beta}^m \\ \boldsymbol{\beta}^c + \Delta\boldsymbol{\beta}^c \end{array} \right\} \\ & = \left[ \begin{array}{cc} \int_{\partial\Omega_e} [\mathbf{P}^m]^T [\mathbf{n}^e] [\mathbf{L}^e] d\partial\Omega & - \int_{\partial\Omega_c} [\mathbf{P}^m]^T [\mathbf{n}^c] [\mathbf{L}^c] d\partial\Omega \\ [\mathbf{0}] & [\mathbf{0}] \end{array} \right] \left\{ \begin{array}{l} \mathbf{q}^e + \Delta\mathbf{q}^e \\ \mathbf{q}^m + \Delta\mathbf{q}^m \\ \mathbf{q}^c + \Delta\mathbf{q}^c \end{array} \right\} \end{aligned}$$

et al. (2000) and Li and Ghosh (2004). Using divergence theorem, the potential energy can be written as

$$\begin{aligned} \Pi_e = & - \int_{\Omega_m} \frac{1}{2} S_{ijkl}^m \Delta\sigma_{ij}^m \Delta\sigma_{kl}^m d\Omega - \int_{\Omega_m} S_{ijkl}^m \sigma_{kl}^m \Delta\sigma_{ij}^m d\Omega \\ & - \int_{\Omega_c} \frac{1}{2} S_{ijkl}^c \Delta\sigma_{ij}^c \Delta\sigma_{kl}^c d\Omega - \int_{\Omega_c} S_{ijkl}^c \sigma_{kl}^c \Delta\sigma_{ij}^c d\Omega \\ & + \int_{\partial\Omega_e} (\sigma_{ij}^m + \Delta\sigma_{ij}^m) n_j^e (u_i^e + \Delta u_i^e) d\partial\Omega \\ & - \int_{\partial\Omega_e^c} (\sigma_{ij}^m + \Delta\sigma_{ij}^m) n_j^c (u_i^m + \Delta u_i^m) d\partial\Omega \\ & + \int_{\partial\Omega_c} (\sigma_{ij}^c + \Delta\sigma_{ij}^c) n_j^c (u_i^c + \Delta u_i^c) d\partial\Omega \\ & - \int_{\partial\Omega_c} \int_{u_n^m - u_n^c}^{u_n^m + \Delta u_n^m - u_n^c - \Delta u_n^c} T_n^m d(u_n^m - u_n^c) d\partial\Omega \\ & - \int_{\partial\Omega_c} \int_{u_t^m - u_t^c}^{u_t^m + \Delta u_t^m - u_t^c - \Delta u_t^c} T_t^m d(u_t^m - u_t^c) d\partial\Omega \\ & - \int_{\Gamma_{tm}} (t_i + \Delta t_i) (u_i^e + \Delta u_i^e) d\Gamma \end{aligned} \tag{21}$$

Here  $\mathbf{n}^e$  and  $\mathbf{n}^c$  are the outward normal on  $\partial\Omega_e$  and  $\partial\Omega_c$  respectively. The integration over the incremen-

or in a condensed form

$$[\mathbf{H}^e] \{ \boldsymbol{\beta} + \Delta\boldsymbol{\beta} \} = [\mathbf{G}^e] \{ \mathbf{q} + \Delta\mathbf{q} \} \tag{23}$$

The weak forms of the global traction continuity conditions are subsequently solved by setting the variation of the total energy function in Eq. (22) with respect to  $\Delta\mathbf{q}$ ,  $\Delta\mathbf{q}^m$  and  $\Delta\mathbf{q}^c$  to zero. This results in the weak form of the traction reciprocity conditions as

$$\begin{aligned} & \sum_{e=1}^{N_{vc}} \left[ \begin{array}{cc} \int_{\partial\Omega_e} [\mathbf{L}^e]^T [\mathbf{n}^e]^T [\mathbf{P}^m] d\partial\Omega & [\mathbf{0}] \\ - \int_{\partial\Omega_m^c} [\mathbf{L}^c]^T [\mathbf{n}^c]^T [\mathbf{P}^m] d\partial\Omega & [\mathbf{0}] \\ [\mathbf{0}] & \int_{\partial\Omega_c} [\mathbf{L}^c]^T [\mathbf{n}^c]^T [\mathbf{P}^c] d\Omega \end{array} \right] \\ & \times \left\{ \begin{array}{l} \boldsymbol{\beta}^m + \Delta\boldsymbol{\beta}^m \\ \boldsymbol{\beta}^c + \Delta\boldsymbol{\beta}^c \end{array} \right\} \\ & = \sum_{e=1}^{N_{vc}} \left\{ \begin{array}{l} \int_{\Gamma_{tm}} [\mathbf{L}^e]^T \{ \bar{\mathbf{t}} + \Delta\bar{\mathbf{t}} \} d\Omega \\ - \int_{\partial\Omega_m^c} [\mathbf{L}^c]^T (\{ \mathbf{n}^c \} T_n^m (u_n + \Delta u_n, u_t + \Delta u_t) \\ + \{ \mathbf{t}^c \} T_t^m (u_n + \Delta u_n, u_t + \Delta u_t)) d\partial\Omega \\ - \int_{\partial\Omega_c} [\mathbf{L}^c]^T (\{ \mathbf{n}^c \} T_n^m (u_n + \Delta u_n, u_t + \Delta u_t) \\ + \{ \mathbf{t}^c \} T_t^m (u_n + \Delta u_n, u_t + \Delta u_t)) d\partial\Omega \end{array} \right\} \end{aligned} \tag{24}$$

or in a condensed form

$$\sum_{e=1}^{N_{vc}} [\mathbf{G}^e]^T \{\boldsymbol{\beta} + \Delta\boldsymbol{\beta}\} = \sum_{e=1}^{N_{vc}} \{\mathbf{R}^e\} \quad (25)$$

Substituting (23) in (25) yields

$$\sum_{e=1}^{N_{vc}} [\mathbf{G}^e]^T [\mathbf{H}^e]^{-1} [\mathbf{G}^e] \{\mathbf{q} + \Delta\mathbf{q}\} = \sum_{e=1}^{N_{vc}} \{\mathbf{R}^e\} \quad (26)$$

In an iterative solution of Eq. (26), its linearized form for the  $i$ th iteration is given as

$$\begin{aligned} & \sum_{e=1}^{N_{vc}} [\mathbf{G}^e]^T [\mathbf{H}^e]^{-1} [\mathbf{G}^e]^i \{\Delta\mathbf{q}\}^i \\ &= \sum_{e=1}^{N_{vc}} \{\mathbf{R}^e\}^i - \sum_{e=1}^{N_{vc}} [\mathbf{G}^e]^T [\mathbf{H}^e]^{-1} [\mathbf{G}^e] \{\mathbf{q} + \Delta\mathbf{q}\}^i \end{aligned} \quad (27)$$

or in a condensed form

$$[\mathbf{K}]^i \{\Delta\mathbf{q}\}^i = \{\Delta\mathbf{F}^{vc}\}^i \quad (28)$$

In order to incorporate this relation in the linearized form of the principle of virtual work of Eq. (13), it should be noted that the displacement vector  $\mathbf{u}_{l2/tr}$  on the boundary of *level-2* and transition element is a subset of all the VCFEM displacement fields, i.e.  $\mathbf{u}^{vc} = \mathbf{u}^e \cup \mathbf{u}^m \cup \mathbf{u}^c$ . Consequently, the displacement field  $\mathbf{u}^{vc}$  can be separated into two categories, viz. (i)  $\mathbf{u}^{l2/tr}$  on nodal points at the boundary of the *level-2* or transition elements shown in Fig. 3, and (ii)  $\mathbf{u}^{int}$  on all the internal nodes. The stiffness matrix and the load vector of the ensemble of all Voronoi cell elements belonging to a *level-2* or transition element can therefore be partitioned as

$$\begin{bmatrix} \mathbf{K}^{l2/tr,l2/tr} & \mathbf{K}^{l2/tr,int} \\ \mathbf{K}^{int,l2/tr} & \mathbf{K}^{int,int} \end{bmatrix}^i \begin{Bmatrix} \Delta\mathbf{q}^{l2/tr} \\ \Delta\mathbf{q}^{int} \end{Bmatrix}^i = \begin{Bmatrix} \Delta\mathbf{F}^{l2/tr} \\ \Delta\mathbf{F}^{int} \end{Bmatrix}^i \quad (29)$$

Static condensation of the internal degrees of freedom yields

$$\begin{aligned} & [[\mathbf{K}^{l2/tr,l2/tr}] - [\mathbf{K}^{l2/tr,int}][\mathbf{K}^{int,int}]^{-1}[\mathbf{K}^{int,l2/tr}]]^i \{\Delta\mathbf{q}^{l2/tr}\}^i \\ &= \{\Delta\mathbf{F}^{l2/tr}\}^i - [\mathbf{K}^{l2/tr,int}][\mathbf{K}^{int,int}]^{-1} \{\Delta\mathbf{F}^{int}\}^i \end{aligned} \quad (30)$$

These stiffness matrices and load vectors are then used in global assembly process of Eq. (13).

### 3.2. Modified voronoi cell FEM formulation for a RVE in level-1 elements

As discussed in Section 2.2, the post-processing phase for *level-1* elements require the evaluation of different variables in the RVE from known values of macroscopic strains. A small variant of the formulation in Eq. (21) enables this execution. The energy functional for a RVE ( $Y$ ) with  $Y$ -periodic displacements and  $Y$ -anti-periodic tractions on the boundary, and imposed macroscopic strain ( $e_{ij} + \Delta e_{ij}$ ), may be written as

$$\begin{aligned} \Pi_e^{RVE} = & - \int_{Y_m} \frac{1}{2} S_{ijkl}^m \Delta\sigma_{ij}^m \Delta\sigma_{kl}^m dY - \int_{Y_m} S_{ijkl}^m \sigma_{kl}^m \Delta\sigma_{ij}^m dY \\ & - \int_{Y_c} \frac{1}{2} S_{ijkl}^c \Delta\sigma_{ij}^c \Delta\sigma_{kl}^c dY - \int_{Y_c} S_{ijkl}^c \sigma_{kl}^c \Delta\sigma_{ij}^c dY \\ & + \int_{\partial Y_e} (\sigma_{ij}^m + \Delta\sigma_{ij}^m) n_j^e (u_i^e + \Delta u_i^e) d\partial Y \\ & - \int_{\partial Y_c^m} (\sigma_{ij}^m + \Delta\sigma_{ij}^m) n_j^c (u_i^m + \Delta u_i^m) d\partial Y \\ & + \int_{\partial Y_c^c} (\sigma_{ij}^c + \Delta\sigma_{ij}^c) n_j^c (u_i^c + \Delta u_i^c) d\partial Y \\ & - \int_{\partial Y_c} \int_{u_n^m - u_n^c}^{u_n^m + \Delta u_n^m - u_n^c - \Delta u_n^c} T_n^m d(u_n^m - u_n^c) d\partial Y \\ & - \int_{\partial Y_c} \int_{u_t^m - u_t^c}^{u_t^m + \Delta u_t^m - u_t^c - \Delta u_t^c} T_t^m d(u_t^m - u_t^c) d\partial Y \\ & + \boxed{\int_{Y_m} (e_{ij} + \Delta e_{ij}) \Delta\sigma_{ij}^m dY + \int_{Y_c} (e_{ij} + \Delta e_{ij}) \Delta\sigma_{ij}^c dY} \end{aligned} \quad (31)$$

The boxed term corresponds to the additional energy due to the imposed macroscopic strain field on the RVE region  $Y$ . The Euler–Lagrange equations corresponding to this energy functional are

$$\begin{aligned} \varepsilon_{ij}(\mathbf{x}, \mathbf{y}) + \Delta\varepsilon_{ij}(\mathbf{x}, \mathbf{y}) &= S_{ijkl}(\sigma_{ij} + \Delta\sigma_{ij}) = (e_{ij}(\mathbf{x}) + \Delta e_{ij}(\mathbf{x})) \\ &+ \frac{1}{2} \left[ \frac{\partial(u_i(\mathbf{y}) + \Delta u_i(\mathbf{y}))}{\partial y_j} + \frac{\partial(u_j(\mathbf{y}) + \Delta u_j(\mathbf{y}))}{\partial y_i} \right] \\ \forall \mathbf{y} \in Y_m, Y_c \end{aligned} \quad (32)$$

$$u_i \text{ is } Y\text{-periodic and } \sigma_{ij}^m n_j^e \text{ is } Y\text{-anti-periodic on } \partial Y_e \quad (33)$$

The corresponding weak form of the element kinematic relation is written in a matrix equation form as

$$\begin{aligned}
& \begin{bmatrix} \int_{\Omega_m} [\mathbf{P}^m]^T [\mathbf{S}^m] [\mathbf{P}^m] d\Omega & [\mathbf{0}] \\ [\mathbf{0}] & \int_{\Omega_c} [\mathbf{P}^c]^T [\mathbf{S}^c] [\mathbf{P}^c] d\Omega \end{bmatrix} \begin{Bmatrix} \boldsymbol{\beta}^m + \Delta \boldsymbol{\beta}^m \\ \boldsymbol{\beta}^c + \Delta \boldsymbol{\beta}^c \end{Bmatrix} \\
& = \begin{bmatrix} \int_{\partial\Omega_e} [\mathbf{P}^m]^T [\mathbf{n}^e] [\mathbf{L}^e] d\partial\Omega & - \int_{\partial\Omega_c} [\mathbf{P}^m]^T [\mathbf{n}^c] [\mathbf{L}^c] d\partial\Omega & [\mathbf{0}] \\ [\mathbf{0}] & [\mathbf{0}] & \int_{\partial\Omega_c} [\mathbf{P}^c]^T [\mathbf{n}^c] [\mathbf{L}^c] d\partial\Omega \end{bmatrix} \begin{Bmatrix} \mathbf{q}^e + \Delta \mathbf{q}^e \\ \mathbf{q}^m + \Delta \mathbf{q}^m \\ \mathbf{q}^c + \Delta \mathbf{q}^c \end{Bmatrix} \\
& - \begin{Bmatrix} \int_{\Omega_m} [\mathbf{P}^m]^T \{\mathbf{e} + \Delta \mathbf{e}\} d\Omega \\ \int_{\Omega_c} [\mathbf{P}^c]^T \{\mathbf{e} + \Delta \mathbf{e}\} d\Omega \end{Bmatrix} \tag{34}
\end{aligned}$$

or in a condensed form

$$[\mathbf{H}^e] \{\boldsymbol{\beta} + \Delta \boldsymbol{\beta}\} = [\mathbf{G}^e] \{\mathbf{q} + \Delta \mathbf{q}\} - \{\mathbf{R}_1^e\} \tag{35}$$

This relation is then substituted in Eq. (25) for obtaining the RVE based solutions. It should be noted that displacement periodicity is imposed on the RVE boundary for solving this problem.

#### 4. Criteria for adaptive mesh refinement and level transitions

In the application of the multi-level model, the following criteria are used for mesh-refinement and level transitions due to discretization and modeling error respectively. Many of these adaptation criteria are based on the physics of the problem in consideration, since rigorous mathematical error bounds are scarce (or even non-existent) for these nonlinear problems. Consequently they are non-unique and other indicators may be used if appropriate.

##### 4.1. Refinement of level-0 and level-1 meshes by *h*-adaptation

The computational models in *level-0* and *level-1* subdomains are enriched by *h*-adaptation based mesh refinement to reduce discretization ‘error’. The *h*-adaptation procedure subdivides candidate macroscopic elements into smaller elements to reduce a suitably chosen error. It is necessary to impose boundary displacement compatibility constraint conditions between contiguous divided and undivided elements in this method (Ghosh et al., 1995). This local mesh enrichment is intended to reduce discretization error and to identify regions of modeling error by zooming in on localization regions with evolving gradients. For CDM based evolving problems, an adaptation criterion is formulated in this paper in terms of the jump in trac-

tion across adjacent element boundaries that signifies local stress gradients. The condition is stated as

Refine element ‘*e*’, if the traction jump error across the element satisfies the condition:  
 $E_e^{tj} \geq C_1 * E_{\text{avg}}^{tj}$ ,

where

$$\begin{aligned}
E_{\text{avg}}^{tj} & = \left( \frac{\sum_{i=1}^{\text{NE}} (E_e^{tj})^2}{\text{NE}} \right)^{1/2} \quad \text{and} \\
(E_e^{tj})^2 & = \frac{\int_{\partial\Omega_e} (|[T_x]|^2 + |[T_y]|^2) d\partial\Omega}{\int_{\partial\Omega_e} d\partial\Omega} \tag{36}
\end{aligned}$$

Here NE is the total number of *level-0* and *level-1* elements in the entire computational domain,  $T_x$ ,  $T_y$  are the components of element boundary tractions in the *x* and *y* directions and  $[[\cdot]]$  is the jump operator across element boundary  $\partial\Omega_e$ . A factor  $C_1$  ( $<1$ ) has been chosen from numerical experiments.

##### 4.2. Criteria for switching from level-0 to level-1 elements

*Level-0* to *level-1* element transition takes place according to criteria signaling departure from conditions of the homogenizability that are based on macroscopic variables in the continuum model of *level-0* elements. The degrading dissipation energy  $W_d$  in the CDM model is a strong indicator of localized damage evolution. Consequently, a criterion is formulated as

Switch element ‘*e*’ from *level-0* to *level-1* if

$$E_e^{\text{gdc}} * (W_d)_e > C_2 * E_{\text{max}}^{\text{gdc}} * (W_d)_{\text{max}} \tag{37}$$

where  $E_i^{\text{gdc}}$  is the norm of the local gradient of the degrading dissipation energy  $(W_d)_e$ , expressed as

$$E_e^{\text{gdc}} = \sqrt{\left(\frac{\partial(W_d)_e}{\partial x_1}\right)^2 + \left(\frac{\partial(W_d)_e}{\partial x_2}\right)^2} \quad (38)$$

$E_{\text{max}}^{\text{gdc}}$  is the maximum value of  $E_e^{\text{gdc}}$  for all elements and  $C_2$  ( $<1$ ) is a prescribed factor. The criterion (37) is helpful for seeking out regions with high gradients of  $W_d$  in regions of high  $W_d$  itself. In a previous paper by the authors (Raghavan and Ghosh, 2004a), the gradient  $E_e^{\text{gdc}}$  was expressed in terms of the maximum difference in the damage for neighboring elements as  $E_e^{\text{gdc}} = \text{Max}|(W_d)_e - (W_d)_{\text{adjacent}}|$ . A more accurate definition of the local gradient is adopted in the present work, using the Zienkiewicz–Zhu (ZZ) gradient patch recovery method (Zienkiewicz and Zhu, 1992). In this method, interpolation of  $W_d$  is assumed in the form of a polynomial over a patch of elements adjoining a nodal point in a *level-0* element. The least square minimization process leads to the local matrix equation

$$\sum_{e=1}^{\text{ne}} [\hat{\mathbf{N}}_e(x_1, x_2)]^T [\hat{\mathbf{N}}_e(x_1, x_2)] \{\mathbf{a}\} = \sum_{e=1}^{\text{ne}} [\hat{\mathbf{N}}_e(x_1, x_2)]^T (W_d)_e(x_1, x_2) \quad (39)$$

where  $[\hat{\mathbf{N}}_e(x_1, x_2)]$  is a matrix containing polynomial interpolation terms and  $\text{ne}$  is the number of elements in the patch. Eq. (39) is solved for the coefficients  $\{\mathbf{a}\}$ . The gradients of  $W_d$  in each element are calculated from the nodal values using element shape functions as

$$\frac{\partial W_d}{\partial x_1} = \sum_{z=1}^4 \frac{\partial N_z}{\partial x_1} (W_d)_z, \quad \frac{\partial W_d}{\partial x_2} = \sum_{z=1}^4 \frac{\partial N_z}{\partial x_2} (W_d)_z \quad (40)$$

### 4.3. Criteria for switching from level-1 to level-2 elements

For elements in which macroscopic nonuniformity has been established according to Eq. (37), departure from RVE periodicity is taken as an indicator for activating a switch from *level-1* to *level-2*. The switching criterion is developed in terms of evolving variables, e.g. the averaged strain at the fiber–matrix interface in the local microstructural RVE. The averaged strain is stated as

$$D_{ij} = \frac{1}{\int_{\cup \partial \Omega_c} d\bar{\Omega}} \int_{\cup \partial \Omega_c} \epsilon_{ij} d\bar{\Omega} = \frac{1}{2 \int_{\cup \partial \Omega_c} d\bar{\Omega}} \int_{\cup \partial \Omega_c} ([u_i]n_j + [u_j]n_i)\Omega_c d\bar{\Omega} \quad (41)$$

where the integral is evaluated over all the fiber–matrix interfaces in the RVE. The jump in displacement across the fiber–matrix interface with a normal  $n_i$  is denoted by  $[u_i]$ . For perfect interfaces  $[u_i]$  will be zero. Thus,  $D_{ij}$  corresponds to the contributions to macroscopic strain due to damage only, and  $D_{ij} = 0$  in the absence of damage. Departure from periodicity will result in a significantly different averaged strain  $D_{ij}$  in response to different conditions on the boundary of the microstructural region. For example, let  $D_{ij}^{e, I2}$  correspond to the solution of a boundary value problem of the local microstructure included in a *level-2* element (see Fig. 2) subject to boundary displacements that have been obtained from the macroscopic *level-0/1* analysis. The scale of the microstructure is relevant in this analysis since periodicity is not imposed on the boundary. On the other hand, let  $D_{ij}^{e, RVE}$  be from the solution of a boundary value problem of the local RVE with imposed macroscopic strains and subjected to periodic boundary displacements constraints. The difference in these two strains for a *level-1* element  $e$  may be quantified as

$$E_e^{\text{dper}} = \max(|D_{11}^{e, I2} - D_{11}^{e, RVE}|, |D_{22}^{e, I2} - D_{22}^{e, RVE}|, |D_{12}^{e, I2} - D_{12}^{e, RVE}|) \quad (42)$$

For evaluating  $D_{ij}^{e, I2}$  in a given step of the incremental solution, only the increments in the present step are calculated by the *level-1* macroscopic displacement boundary conditions. It is assumed that the RVE-based solution is valid all the way upto (but excluding) the present step. The departure from periodicity is measured in terms of the difference in averaged strains  $E_e^{\text{dper}}$ , and hence the criterion,

Switch element ‘ $e$ ’ from *level-1* to *level-2* if

$$E_e^{\text{dper}} > C_3 D_{\text{max}}^{\text{RVE}} \quad (43)$$

where  $D_{\text{max}}^{\text{RVE}}$  is the maximum value of  $|D_{ij}^{e, RVE}|$  for all the *level-1* elements in the computational domain.

**Remark.** Once the regions of *level-2* and *transition* elements have been identified, it is important to update the local micromechanical states of stress, strain and damage to the current state. This step should precede the coupled concurrent analysis. For this analysis, the history of the macroscopic displacement solution on the *level-0/level-1* element boundary prior to the switch is utilized. The local micromechanical (VCFEM) boundary value problem for the *level-2* element is incrementally solved

from the beginning to obtain the history of stresses, strains and damage in the microstructure from the macroscopic boundary displacement history.

**5. Numerical examples with the adaptive multilevel model**

Two sets of numerical examples are solved to study the effectiveness of the multi-level computational model for composite materials.

*5.1. Multi-level model vs. micromechanical analysis*

This example is aimed at understanding the effectiveness of the multi-level model in analyzing a non-uniform composite microstructure by comparing its predictions with those by pure micromechanical analysis. It is computationally intensive to conduct pure micromechanical analysis with evolving damage for very large microstructural regions. Consequently a computational domain with a small population of fibers, as shown in the optical micrograph of Fig. 5(a), is considered. The micrograph is for a polymer matrix composite with a random dispersion of uniaxial fibers. The dimensions of the micrograph analyzed are  $100\ \mu\text{m} \times 70.09\ \mu\text{m}$ , containing 264 circular fibers of diameter  $1.645\ \mu\text{m}$  each, corresponding to a volume fraction of 32%.

Though the domain may not be adequate for a clear separation between continuum and micromechanical regions (since relatively large regions are needed to materialize the RVE), the results of this example are enough to show the effectiveness of the overall framework.

The optical micrograph is mapped onto a simulated microstructure with circular fibers that is tessellated into a mesh of 264 Voronoi cell elements, as shown in Fig. 5(b). The constituent materials in the composite system are an epoxy resin matrix, stainless steel reinforcing fibers and a very thin film of freekote ( $<0.1\ \mu\text{m}$ ) at the fiber–matrix interface. The freekote imparts a weak strength to the steel–epoxy interface, which allows a stable growth of the debond crack for experimental observation. The experimental methods of material and interface characterization have been discussed in Ghosh et al. (2000). Both the matrix and fiber materials are characterized by isotropic elasticity properties. The matrix material has a Young’s modulus,  $E_{\text{epoxy}} = 4.6\ \text{GPa}$  and Poisson’s ratio,  $\nu_{\text{epoxy}} = 0.4$ , while the fiber material has a Young’s modulus,  $E_{\text{steel}} = 210\ \text{GPa}$  and Poisson’s ratio,  $\nu_{\text{steel}} = 0.3$ . A bilinear cohesive law described in Li and Ghosh (2004) and Ortiz and Pandolfi (1999) is used in this analysis for modeling the fiber–matrix interface. In this model, the normal and tangential tractions are given as

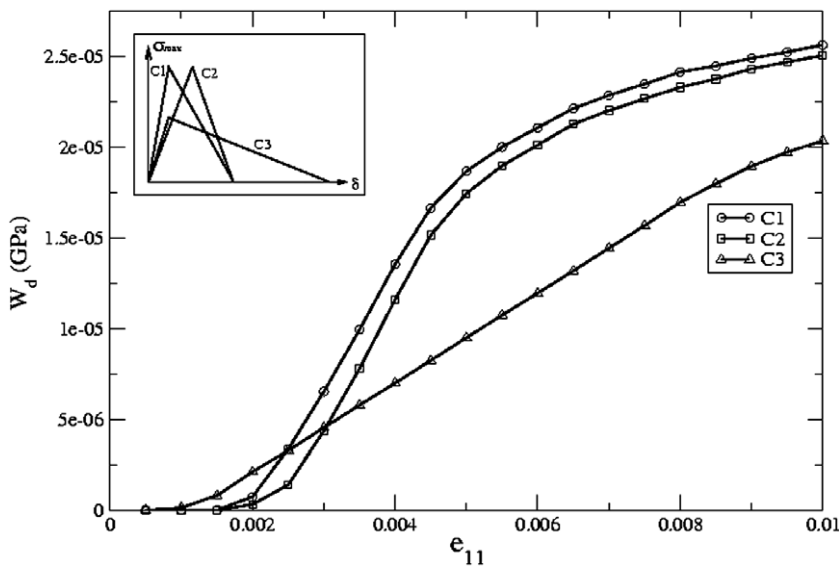


Fig. 4. The degrading dissipation energy  $W_d$  as a function of strain, evaluated for different cohesive zone parameters in the bilinear cohesive law.

$$T_n = \frac{\partial \phi}{\partial \delta_n} = \frac{\partial \phi}{\partial \delta} \frac{\partial \delta}{\partial \delta_n} = \begin{cases} t \delta_n & \text{if } \delta \leq \delta_c \\ t \delta_n & \text{if } \delta_c < \delta \leq \delta_e \\ 0 & \text{if } \delta > \delta_e \end{cases}$$

$$T_t = \frac{\partial \phi}{\partial \delta_t} = \frac{\partial \phi}{\partial \delta} \frac{\partial \delta}{\partial \delta_t} = \begin{cases} t \beta^2 \delta_t & \text{if } \delta < \delta_c \\ t \beta^2 \delta_t & \text{if } \delta_c < \delta \leq \delta_e \\ 0 & \text{if } \delta > \delta_e \end{cases} \quad (44)$$

where  $t$  is a bilinear function of the interfacial separation as

$$t = \begin{cases} \frac{\sigma_{\max}}{\delta_c} \delta & \forall \delta < \delta_c \\ \frac{\delta - \delta_e}{\delta_c - \delta_e} \sigma_{\max} & \forall \delta \geq \delta_c \end{cases} \quad (45)$$

The unloading behavior in the hardening region is linear following the loading path. In the softening region, the unloading proceeds along a different linear path from the current position to the origin with a reduced stiffness, for which the  $t - \delta$  relation is

$$t = \frac{\sigma_{\max}}{\delta_{\max}} \frac{\delta_{\max} - \delta_e}{\delta_c - \delta_e} \delta, \quad \delta_c < \delta_{\max} < \delta_e \text{ and } \delta < \delta_{\max} \quad (46)$$

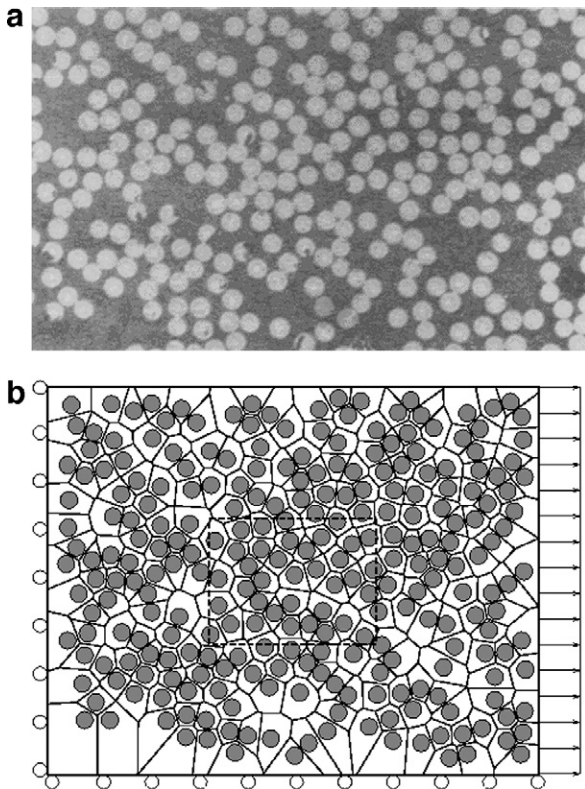


Fig. 5. (a) Optical micrograph of a steel fiber–epoxy matrix composite with 264 fibers and (b) the simulated computational model with a Voronoi cell mesh.

It is expected that the degrading dissipation energy  $W_d$  in the macroscopic CDM model depends on the cohesive parameters in the microstructural debonding model. A square RVE with a single circular fiber is simulated for interfacial debonding with three different sets of cohesive parameters, as shown in the inset of Fig. 4. The cohesive energies are the same for all cases. However in one case, the critical separation length  $\delta_e$  is increased while in the other, the corresponding peak stress  $\sigma_{\max}$  is reduced. Fig. 4 infers that while  $\delta_e$  has a small influence on  $W_d$ , the effect of  $\sigma_{\max}$  is certainly significant, at least in the early stages of straining.

The cohesive parameters used in this paper are:  $\sigma_{\max} = 0.005$  GPa,  $\delta_c = 5.1 \times 10^{-5}$  m and  $\delta_e = 3.1 \times 10^{-4}$  m. The microstructure is loaded in tension in the horizontal direction with a displacement

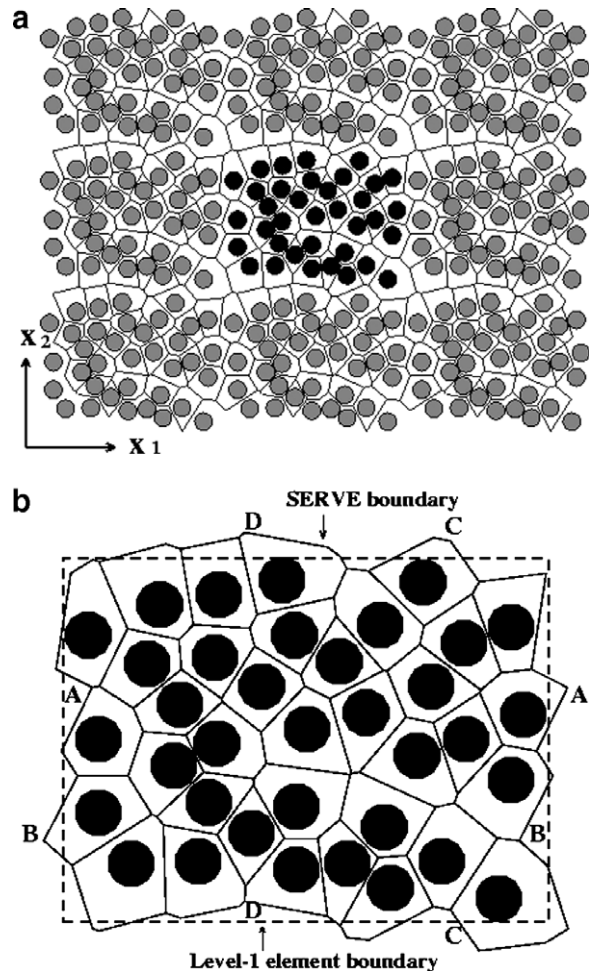


Fig. 6. (a) A periodic microstructure containing the tessellated RVE (fibers in black) and (b) placement of the RVE in the level-1 element showing periodic nodes on the boundary.

of 0.1  $\mu\text{m}$  that is uniformly increased in 20 equal increments, corresponding to a total strain of  $\epsilon_{11} = 0.1\%$ . The displacement boundary condition is imposed along the right edge, as shown in Fig. 5(b).

5.1.1. Micromechanical analysis by VCFEM

The pure micromechanical VCFEM solution using the mesh of Fig. 5(b) has been presented in Li and Ghosh (2004) and are used here as reference solutions for the multi-scale simulation. Fig. 8(a) shows the contour plot of microscopic stress  $\sigma_{xx}$  at the final step of the micromechanical simulation with a depiction of interfacial debonding. The right side of the microstructure shows significant concen-

trated damage with this load. The debonding initiates at the top and percolates to the bottom of the microstructure along a narrow band.

5.1.2. Multi-scale analysis with the multi-level model

Multi-scale analysis is performed by the concurrent multi-level computational model and the results

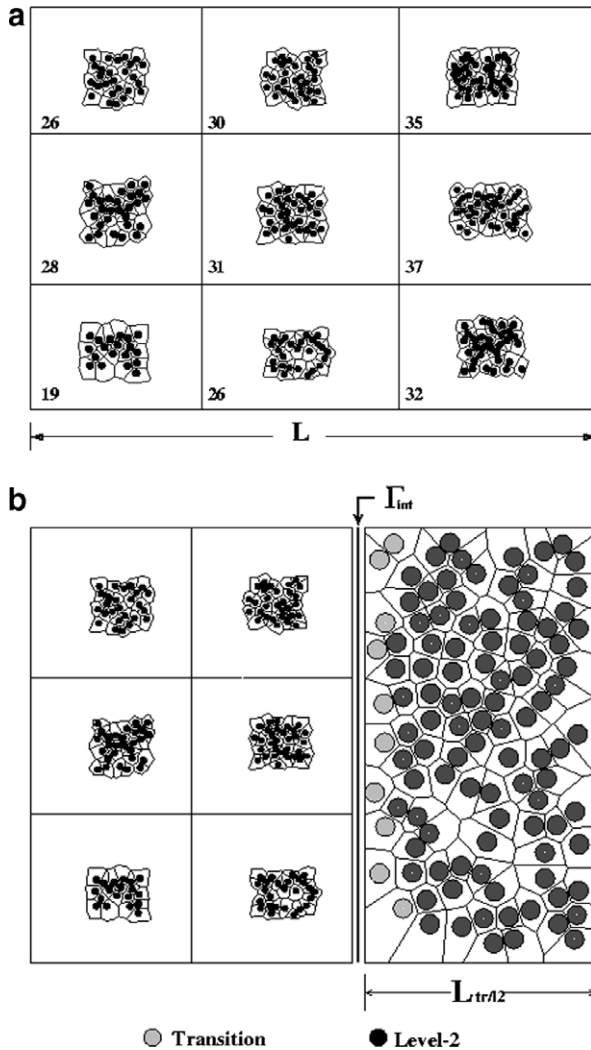


Fig. 7. Computational mesh for the computational domain: (a) macroscopic mesh with different RVE in every element and (b) multi-level model with the interface between macroscopic and microscopic VCFE elements.

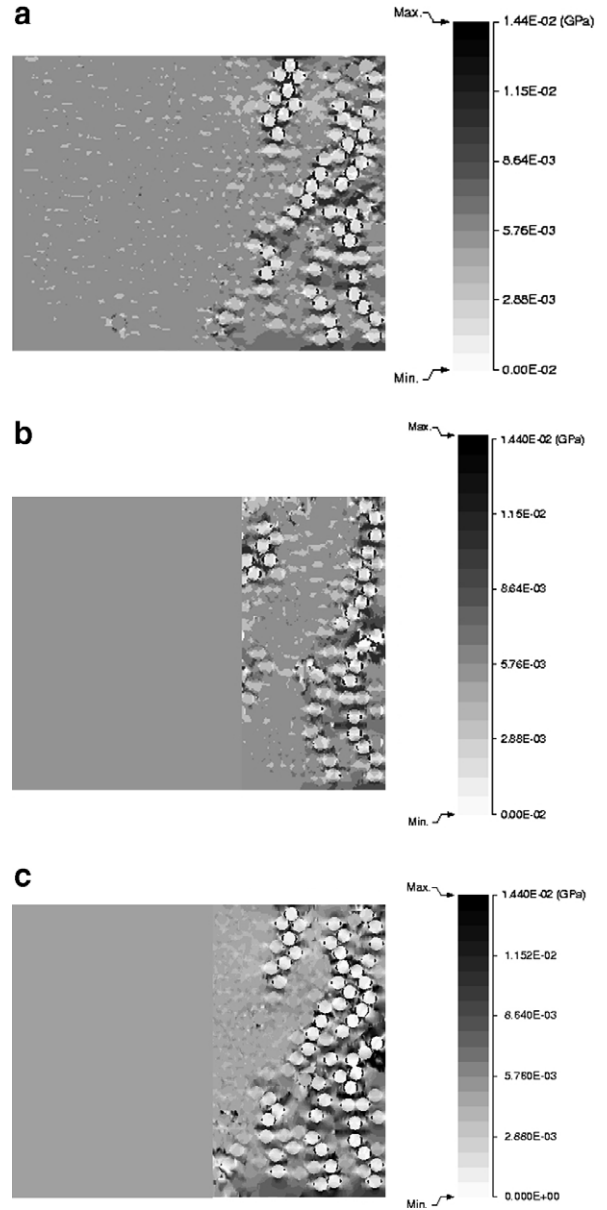


Fig. 8. Contour plot of  $\sigma_{11}$  showing interfacial debonding at the end of the simulation, for: (a) pure micromechanical analysis, (b) analysis by multi-scale model with a smaller *level-2* region ( $\frac{L_{tr/12}}{L} = 0.35$ ), and (c) analysis by multi-scale model with a larger *level-2* region ( $\frac{L_{tr/12}}{L} = 0.45$ ).

are compared with those from the micromechanical VCFEM analysis. For the multi-level model, the entire computational region of 264 fibers is first divided into nine macroscopic finite elements as shown in Fig. 7(a). For evaluating the homogenized constitutive properties for each of element, statistically equivalent representative volume element or SERVE for the microstructure underlying each macroscopic element is first identified. Various statistical methods have been used to determine the size scale of the RVE and the number of inclusions contained in it (Pyrz, 1994; Ghosh et al., 1997; Shan and Gokhale, 2002; Bulsara et al., 1999). Rigorous methods of evaluating statistically equivalent representative volume elements by a combination of statistical methods and micromechanical analyses have been conducted by the first author in Swaminathan et al. (2006a,b). However, since the number of fibers in the micrograph is limited in this exercise, a simpler assumption is made. The SERVE for each element is assumed to consist of all the fibers belonging to that element. For example, to generate the SERVE for an element window in the micrograph of Fig. 5(b), all fibers whose centers are located within this window are first identified as constituents of the RVE. This is shown by the aggregate of black fibers in Fig. 6(a). The homogenization method, discussed in Sections 2.2 and 3, requires a periodic distribution of the RVE and this is achieved by locally repeating the arrangement of fibers in both the  $x_1$  and  $x_2$  directions for a period

length in Fig. 6(a). This means that for each fiber identified in the element, at  $(x_1, x_2)$ , four identical fibers are placed at the locations  $(x_1 \pm X_1, x_2)$ ,  $(x_1, x_2 \pm X_2)$  where  $(X_1, X_2)$  are periods in the two directions. The period lengths  $X_1, X_2$  are selected such that the volume fraction of RVE matches that of the local microstructure. Finally, the domain is tessellated into a network of Voronoi cells as shown in Fig. 6(b) Tessellation provides a natural way of creating periodic SERVE boundary. For non-uniform fiber arrangements, the SERVE boundary consists of non-straight line edges. The nodes on this SERVE boundary are periodic, i.e. for every boundary node a periodic pair can be identified on the boundary at a distance of one period along each of the coordinate directions. In Fig. 6(b), the node pairs are identified as AA, BB etc. The number of fibers and their distribution in the SERVE of each macroscopic element is shown in Fig. 7(a).

Since the number of elements in this exercise is very small (only 9), *level-0* simulations with the CDM model is bypassed in the multi-level analysis. All elements are *level-1* at the start of the multi-level simulation. Switch to *level-2* elements is made in accordance with Eqs. (42) and (43) with  $C_2 = 0.2$ . However the  $D_{ij}^{e,l2} - D_{ij}^{e,RVE}$  terms for each element in Eq. (42) are replaced by the difference in RVE based averaged strains between adjacent elements  $D_{ij}^{1,RVE} - D_{ij}^{2,RVE}$ . Also, as opposed to an entire macroscopic element, a single layer of transition Voronoi cell elements is included between the

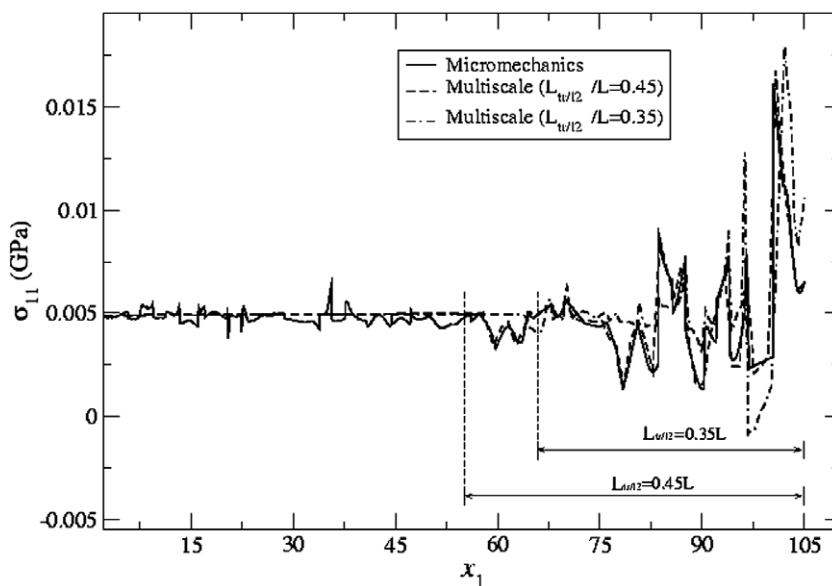


Fig. 9. Comparison of microscopic stress  $\sigma_{11}$  by different methods, plotted along a line through the middle of microstructure.

level-1 and level-2 elements. In Fig. 7(b) the Voronoi elements containing the grey fibers constitute the transition layer, while those containing the black fibers belong to level-2. An interface segment  $\Gamma_{\text{int}}$  is inserted between the transition and level-1 elements at a distance  $L_{\text{tr}/12}$  from the right edge. Convergence properties of the multi-level model are studied by considering two cases with  $\frac{L_{\text{tr}/12}}{L} = 0.35$  and  $\frac{L_{\text{tr}/12}}{L} = 0.45$ . This is achieved by changing the size of the initial level-1 elements.

As depicted in Fig. 7(b), only three elements (3, 6 and 9) at the right side of the initial mesh switch

from level-1 to level-2. A comparison of results by (a) VCFEM based micromechanical analyses (all level-2 elements), (b) homogenization based macroscopic analysis (all level-1 elements), and (c) concurrent multi-level analysis (level-1 and level-2 elements) for  $\frac{L_{\text{tr}/12}}{L} = 0.35$  and 0.45 is made. Contour plots of  $\sigma_{11}$  (GPa) showing interfacial debonding at the end of the simulation are shown for the concurrent multi-scale analysis in Fig. 8(b) and (c). The discrepancy in the damage path predicted by the micromechanical analysis and the multi-level analysis reduces sharply with increasing  $\frac{L_{\text{tr}/12}}{L}$  value. This

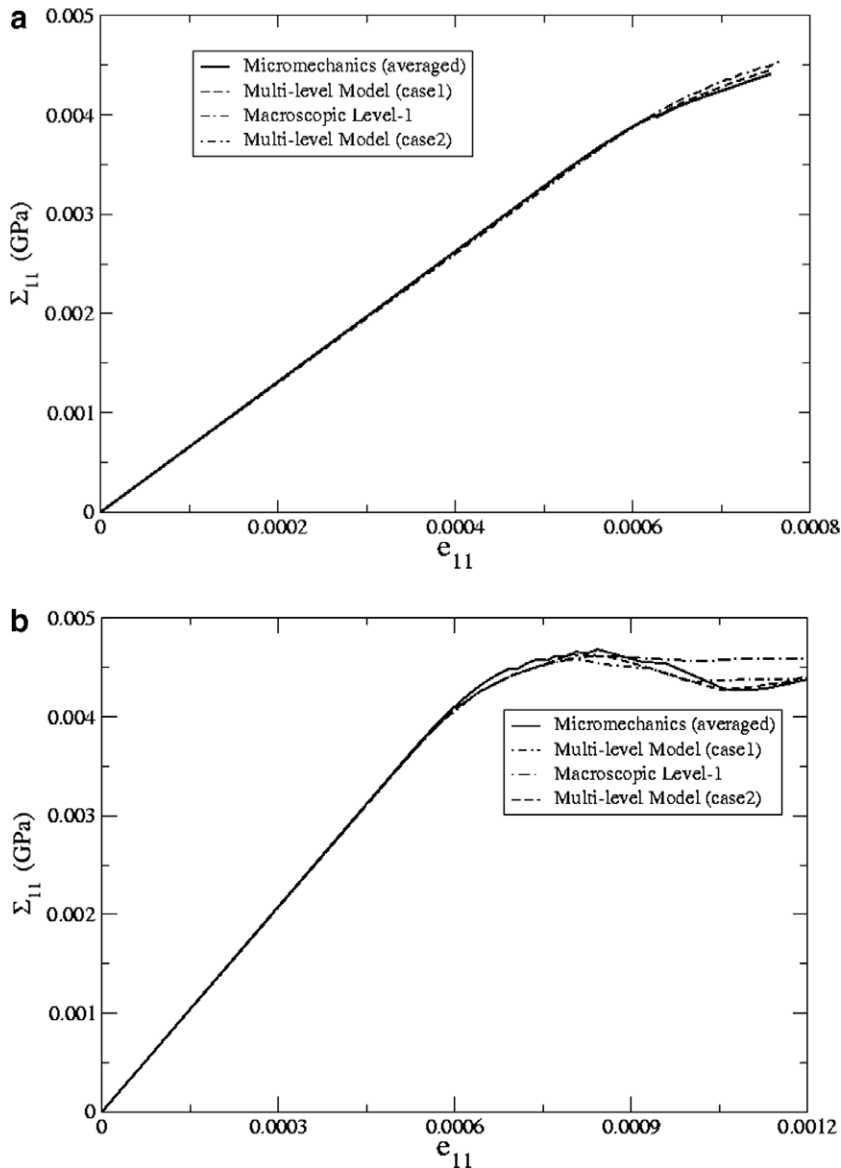


Fig. 10. Comparison of macroscopic (volume averaged)  $\Sigma_{11} - e_{11}$  curves by different methods of analysis at (a) macroscopic element 1 and (b) macroscopic element 9.

can be attributed to the fact, that the damage path is very sensitive to the macro–micro interface conditions. Since the sample size is small and there is no real periodicity in the microstructure, the proximity of the *level-1* boundary to the damage localization zone alters the local boundary conditions. However as this distance is increased, the microscopic stress distribution, debonding pattern and damage zone replicates the real event observed in micromechanical analysis. The distribution of the micromechanical stresses  $\sigma_{11}$ , generated by pure micromechanical and multi-level analyses, are plotted along a line through the middle of micrograph in Fig. 9. The micromechanical stresses show only minor oscillations about an averaged value of the 0.005 GPa in the region to the left of the *level-1*–*level-2* interface. In the region to the right, where damage is predominant, there is clearly a convergence of the stresses with increasing  $\frac{L_{cr}/l_2}{L}$  value.

The macroscopic or averaged stress–strain response for element 1 (always *level-1*) and element 9 (changes levels) are plotted in Fig. 10. For the micromechanical problems with debonding, the volume averaged stresses and strains are evaluated by averaging the local fields over the microscopic domain as

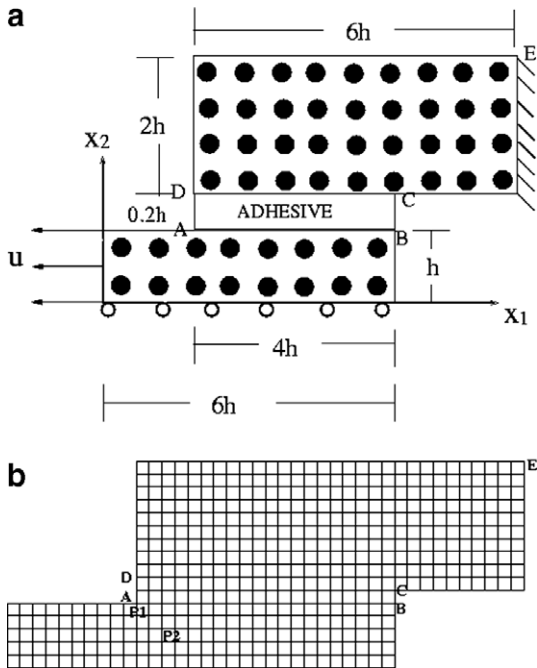


Fig. 11. (a) Schematic diagram of a composite double lap joint showing dimensions and boundary conditions and (b) the *level-0* computational mesh.

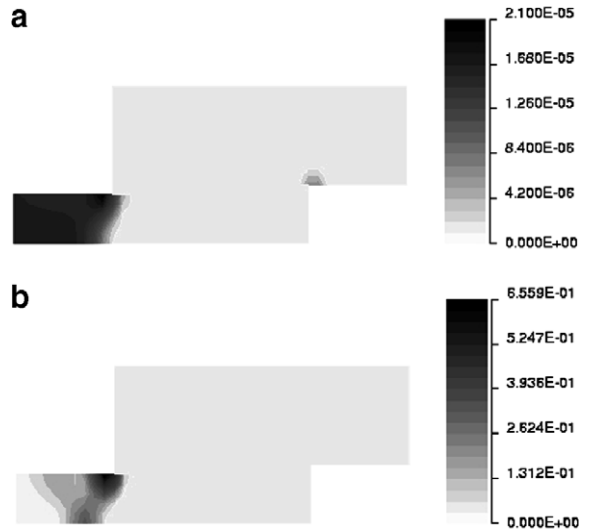


Fig. 12. Contour plot of (a) degrading dissipation energy  $W_d$  and (b) its gradient  $\sqrt{\left(\frac{\partial W_d}{\partial x_1}\right)^2 + \left(\frac{\partial W_d}{\partial x_2}\right)^2}$  at the final loading stage.

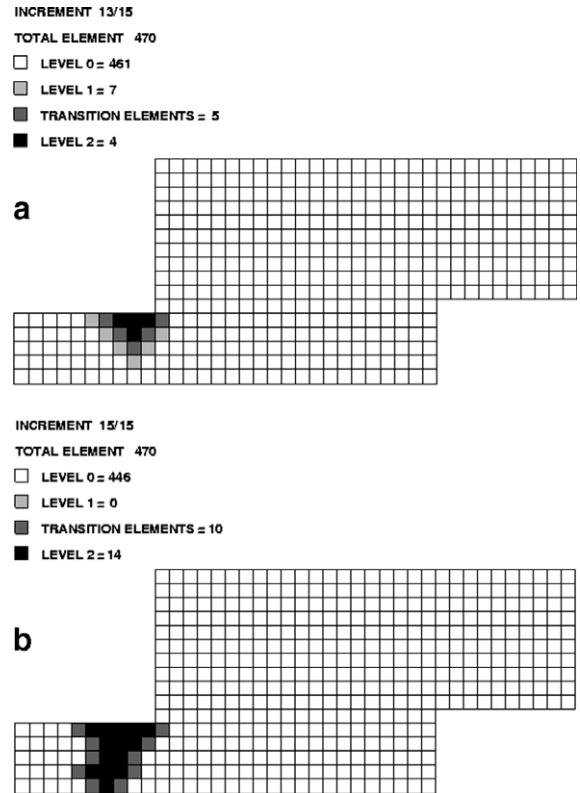


Fig. 13. Evolution of the multi-level computational model with level transition (a) at 87% loading and (b) at the final loading stage.

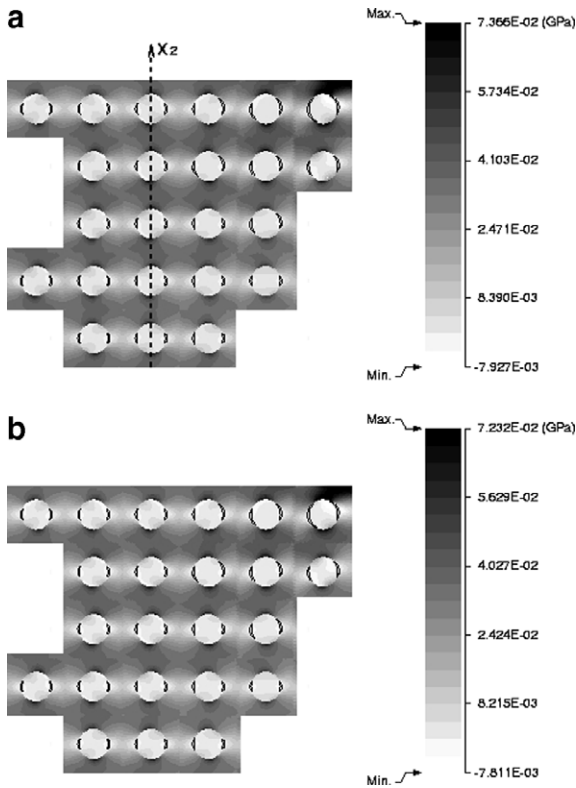


Fig. 14. Level 2 microscopic VCFEM elements near the corner A showing microscopic stress distribution (GPa) and interfacial debonding at the end of the analysis by: (a) pure micromechanical analysis and (b) multi-scale analysis.

$$\Sigma_{ij} = \frac{1}{\Omega} \int_{\Omega} \sigma_{ij}(x_1, x_2) d\Omega \quad \text{and}$$

$$e_{ij} = \frac{1}{\Omega} \int_{\Omega} \epsilon_{ij}(x_1, x_2) d\Omega - D_{ij} \quad (47)$$

where  $D_{ij}$  is the strain jump defined in Eq. (41). The results for all the models are in good agreement for the element 1, where there is no significant microstructural damage. The small difference is due to the periodicity constraints imposed on the microstructure. Also there is a difference between the results of case 1:  $\frac{L_{tr}/l_2}{L} = 0.35$  and case 2:  $\frac{L_{tr}/l_2}{L} = 0.45$ , due to the interface conditions at  $\Gamma_{int}$ . However, as is expected the results are quite different for element 9, where significant damage is observed in Fig. 8. The level-1 analysis shows significant deviation from the micromechanical analysis due to imposed periodicity in the damage zone. Once again, the results improve significantly with increasing  $\frac{L_{tr}/l_2}{L}$  ratio.

5.2. A composite double lap joint with microstructural debonding

Adhesive bonded joints are considered as preferred alternatives to fasteners for joining structural components due to their light weight. However, adhesively bonded structures consisting of different materials, can induce high stresses near the interface leading to failure initiation by interfacial debond-

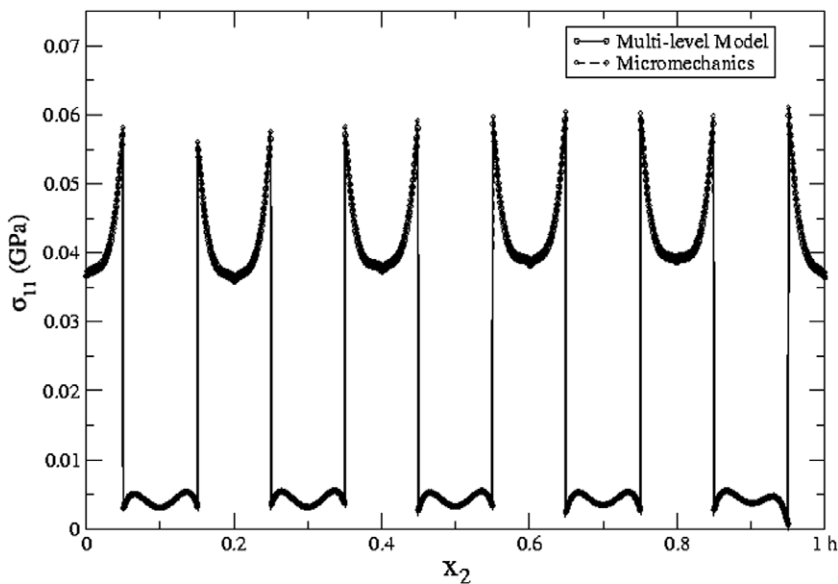


Fig. 15. Stress distribution along the vertical dashed line shown in Fig. 14(a).

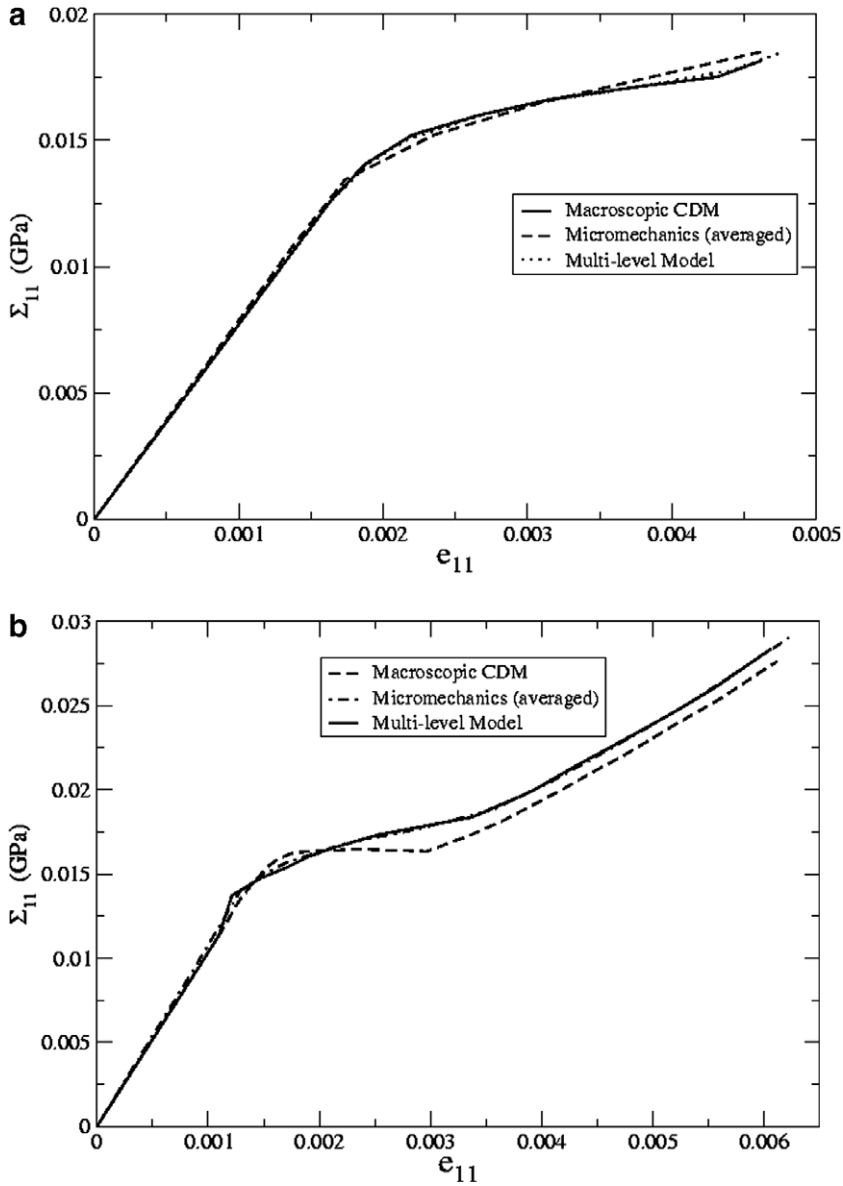


Fig. 16. Macroscopic averaged stress–strain ( $\Sigma_{11} - e_{11}$ ) plot by different methods at two locations: (a) P2 and (b) P1.

ing. A double-lap bonded joint with boron–epoxy composites as adherents, is analyzed in this example. An adhesive shown as ABCD in Fig. 11(a) is used to bond the two composite materials. Only a quarter of the joint is modeled from considerations of symmetry in boundary and loading conditions. For boundary conditions, the displacement component  $u_1$  is set to zero along the face  $x_2 = 0$  implying symmetry about the  $x_1$  axis. The displacement components  $u_1$  and  $u_2$  along the face  $x_1 = 8h$  are set to zero corresponding to a fixed edge. A tensile displacement  $u_1$  is applied on the face of the lower

Table 1  
CPU time on a IA32 cluster to solve the double lap joint model by various methods

Model	Level-0	Level-1	Micromechanics (Level-2)	Multi-scale
Time (s)	71	300,330	300,310	42,260

ply at  $x_1 = 0$ . Both plies above and below the adhesive are made of unidirectional boron fiber–epoxy matrix composite materials. The fibers are uniformly arranged in a square array in the microstructure, implying a square unit cell with a single

circular fiber. The epoxy matrix has a Young's modulus  $E = 4.6$  GPa and Poisson's ratio  $\nu = 0.4$ , while boron fibers have a Young's modulus  $E = 210$  GPa and Poisson's ratio  $\nu = 0.3$ . The material properties of the isotropic adhesive are: Young's modulus  $E = 3.45$  GPa and Poisson's ratio  $\nu = 0.34$ . The bilinear cohesive law parameters for the matrix–fiber interface are:  $\sigma_{\max} = 0.02$  GPa,  $\delta_c = 5.0 \times 10^{-5}$  m and  $\delta_e = 20.0 \times 10^{-4}$  m.

### 5.2.1. Multi-level analysis for model with 450 fibers

In this model, the top ply above the adhesive consists of 10 rows of fiber, while the bottom row consists of five rows resulting in a total of 450 fibers. The microstructural volume fraction of fibers is  $V_f = 20\%$ . The applied displacement on the face at  $x_1 = 0$ , is uniformly increased from zero to  $u_1 = 1.2 \times 10^{-3}$  h in 15 uniform increments. The number of fibers is kept low in this example, such that a micromechanical analysis can be easily done for this example with a mesh of 450 Voronoi elements, each of which is a square unit cell. The micromechanics solutions are used as a reference to determine the accuracy of multi-scale simulations. Three different approaches are used to solve this problem. They are: (a) a macroscopic model using the continuum damage model for constitutive behavior, (b) a detailed micromechanical VCFEM analysis, and (c) a multi-level model for multi-scale analysis. The starting mesh in the multi-level model of the bonded joint consists of a uniform grid of 470 QUAD4 elements for macroscopic analysis as shown in Fig. 11. The constitutive relation for each element is a fourth order anisotropic CDM model that has been developed for this unit cell with interfacial cohesive zone in Raghavan and Ghosh (2005). Fig. 12(a) shows the contour of degrading dissipation energy  $W_d$ , at the final stage of loading by a pure CDM based macroscopic analysis. Damage initiates near the bottom left corner A of the adhesive joint and propagates downwards to span the entire region on the left of point A. *Level-0*  $\rightarrow$  *level-1* transition in the multi-level analysis is performed using Eq. (37) and *level-1*  $\rightarrow$  *level-2* transition uses Eq. (43) with factors  $C_2 = 0.5$  and  $C_3 = 0.1$ . The gradient of the energy  $\sqrt{\left(\frac{\partial W_d}{\partial x_1}\right)^2 + \left(\frac{\partial W_d}{\partial x_2}\right)^2}$  at the final loading stage, used in Eq. (37), is shown in Fig. 12(b). The corresponding evolution of various levels in the multi-scale model is depicted in Fig. 13 at two different loading stages. There are seven *level-1* elements at 87% of

the final loading. At the final load increment, the multi-level mesh consists of 446 *level-0* elements, 0 *level-1* elements, 14 *level-2* elements and 10 *transition* elements. All *level-2* elements emerge in critical regions where both the gradient and intensity of  $W_d$  are high in the macroscopic analysis. Fig. 14(a) and (b) depict the contours of microscopic stress  $\sigma_{11}$  and the regions of debonding obtained by pure micromechanical and the multi-level models. The results of the multi-level model are in excellent agreement with the micromechanical analysis, both with respect to debonding regions and evolving variables. The maximum error in  $\sigma_{11}$  is around 1%. The excellent agreement is further corroborated in the plot of  $\sigma_{11}$  along the vertical line through the microstructure in Fig. 15. Fig. 16(a) and (b) plot the macroscopic (averaged)  $\Sigma_{11} - e_{11}$  curve obtained from (a) macroscopic CDM-based analysis, (b) micromechanical analysis and (c) multi-scale analysis with the multi-level model at two different locations, P1 and P2 shown in Fig. 11(b). At P2, where the damage and its gradient are low, solutions

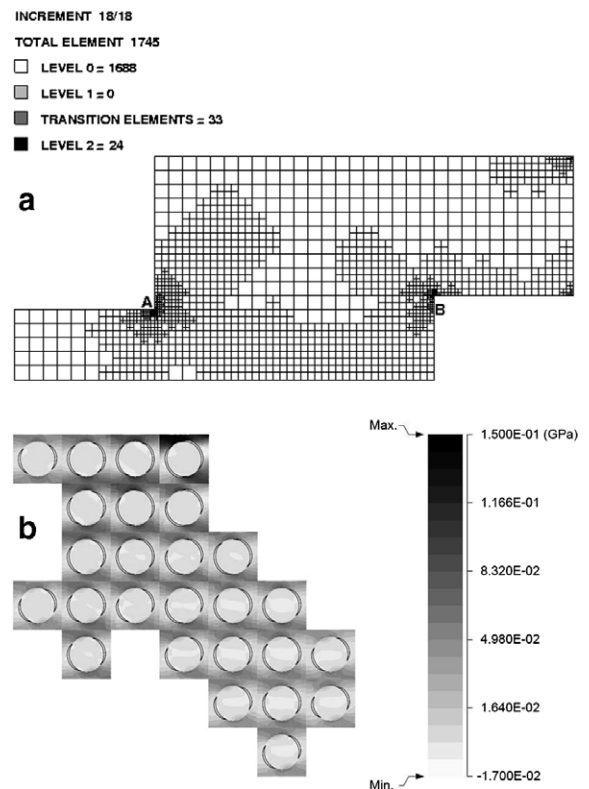


Fig. 17. (a) Evolved multi-level model and mesh at the final load step and (b) microscopic stress distribution and interfacial debonding at the end of analysis for location near corner A, for  $V_f = 40\%$  and case C1.

by the CDM model and micromechanics are in relatively good agreement. At this point, the multi-scale model uses the CDM constitutive law. However, the CDM results are quite different from the other two at P1, a hotspot where the damage and its gradient are high. It is assuring to note that the multi-level model matches the micromechanics results quite well at this point.

The computational efficiency of the multi-level model is examined by a comparison of the CPU time

on a IA32 computer cluster for the different models. The computations are carried out in a serial manner using a single processor. The results are tabulated in Table 1. Although the macroscopic CDM analysis is faster, it can lead to significant errors. The complete *level-1* solution is even slower than the micromechanics solution, since it solves the RVE problem in every element. Accurate analysis with the multi-level model is at least seven times faster than the complete micromechanics and *level-1* solutions for

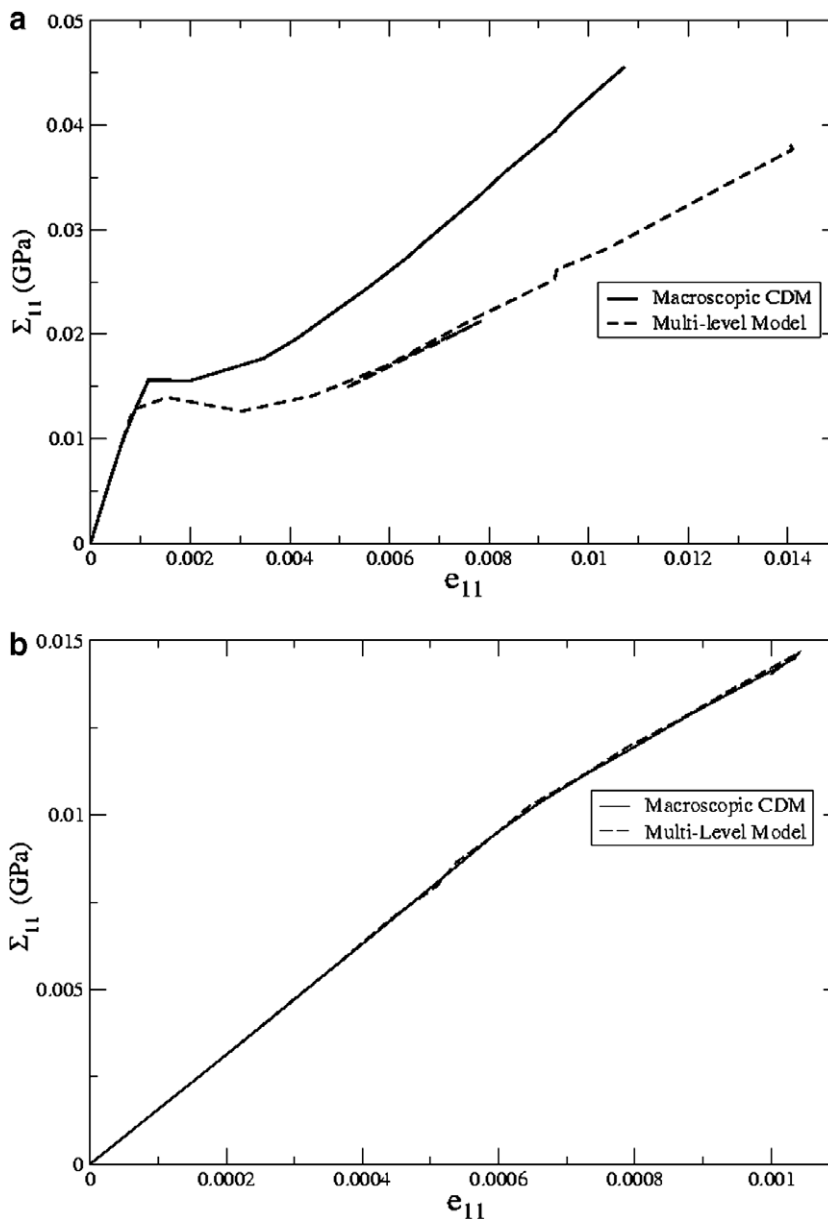


Fig. 18. Macroscopic averaged stress–strain ( $\Sigma_{11} - e_{11}$ ) plot at two locations in the double lap joint: (a) critical region A and (b) non-critical region B.

this problem. The efficiency increases rapidly with increasing number of fibers in the analysis.

### 5.2.2. Multi-level analysis for model with 192,000 fibers

This is a more realistic model of the composite joint with a large number of fibers, to realize the potential of the multi-level model. The top ply consists of 160 rows of fiber, while the bottom row consists of 80 rows resulting in a total of 192,000 fibers. The geometric and material parameters are the same as in the previous example, except for the special cases mentioned. A pure micromechanical analysis is not conducted due to the large number of fibers. The problem is analyzed by (a) a macroscopic model by CDM and (b) the multi-level model. The multi-level analysis activates all three types of adaptation:

- Refinement of *level-0* elements by *h*-adaptation in accordance with Eq. (36), for  $C_1 = 0.7$ .
- Transition from *level-0* to *level-1* elements in accordance with Eq. (37), with  $C_2 = 0.5$ .
- Transition from *level-1* to *level-2* elements in accordance with Eq. (43), with  $C_3 = 0.1$ .

The effects of variation of cohesive zone parameters and the effect of volume fraction are studied. The unit cells considered in this example have two volume fractions: (i)  $V_f = 20\%$  and (ii)  $V_f = 40\%$ .

Three different cases with different parameters in the bilinear cohesive law are considered.

- *C1*: Same cohesive parameters as in Section 5.2.1.
- *C2*:  $\sigma_{\max}$  and  $\delta_e$  are the same as in Section 5.2.1. However,  $\delta_c$  is four times that in case *C1*. This reflects the same cohesive energy with a smaller ascending slope.
- *C3*:  $\sigma_{\max}$  is reduced by half and  $\delta_e$  is doubled. Hence the cohesive energy is the same as *C1* with a smaller peak stress. Also  $\delta_c$  is the same as that in *C1*.

The starting mesh has 470 *level-0* elements. For  $V_f = 40\%$  and case *C1*, the final mesh has 1688 *level-0* elements, 24 *level-2* elements and 33 *transition* elements as shown in Fig. 17(a). Fig. 17(b) illustrates the corresponding microscopic stress distribution and debonding in the *level-2* regions near the hotspot at A. The macroscopic (averaged). Stress–strain plots are shown for two points in the composite joint: (a) near the critical point A and (b) at a non critical point B are shown in Fig. 18. The predictions of the CDM model agree with the multi-level model at the point B. However, the stress predictions by the CDM model are considerably higher than those by the multi-level model at A, where damage is very localized and the periodicity condition imposed by the CDM model is unrealistic.

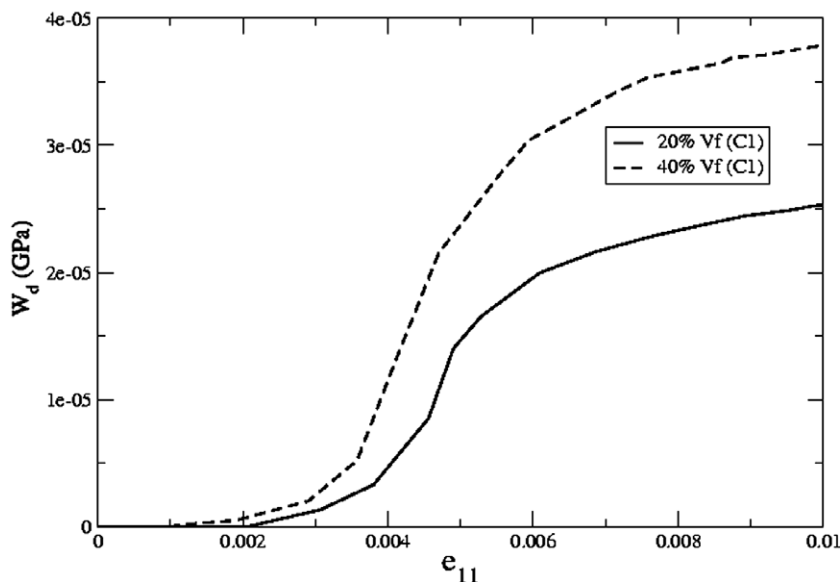


Fig. 19. Degrading dissipation energy evolution near the corner A of the double lap joint for  $V_f = 20\%$  and  $V_f = 40\%$ , and case *C1*.

The effect of  $V_f$  on the damage evolution near the corner P1 is seen in Fig. 19 for the case C1. A significantly higher  $W_d$  is observed for the higher volume fraction, which increases with evolving strain. Fig. 20 shows the distribution of  $W_d$  at the end of the analysis for the different cohesive parameters. Intense damage localization takes place near the junction A in the bond (see Fig. 11(b)). Damage starts from this location and propagates down and left towards the edge of the applied loading. Damage localization is the strongest for the case C1, and propagates almost vertically down in a narrow zone. It is in these regions, that scale transition to *level-2* occurs. The damage distribution in the remaining parts of the composite joint is rather low and uniform. Moving the peak stress in case C2 with a lower traction-displacement slope results in a more diffused damage region and the damage seem to spread more in the region to the left of point A. The damage localization reduces for the case C3 with lower peak stress and the damage is more

evenly distributed. For  $V_f = 20\%$ , the damaged regions are less localized.

## 6. Conclusions

An adaptive concurrent multi-level computational model is developed in this paper for multi-scale analysis and prediction of damage in fiber reinforced composite materials. Microstructural damage is manifested by fiber–matrix interfacial debonding in this paper. Microstructural damage mechanisms leading to complete failure are more complex than the singular mode of damage considered in this paper. The authors are currently working towards this goal, where interfacial debonds bifurcate into the matrix and eventually coalesce to cause a continuous fracture path. A step forward in this direction can be seen in a recent paper on the growth and coalescence of multiple cohesive cracks (Li and Ghosh, 2006). However, the intent of the present paper is to create a framework for the multi-scale coupling so that more complex damage mechanisms may eventually be incorporated. Hence interfacial debonding is deemed sufficient for this purpose.

The multi-level model invokes two-way coupling of scales, viz. a bottom-up coupling with homogenization at lower scales to introduce reduced order continuum models and a top-down coupling at critical hotspots to transcend scales for following the microstructural damage evolution. The bottom-up coupling results in a continuum damage mechanics (CDM) model developed in a preceding paper (Raghavan and Ghosh, 2005). Three levels of hierarchy, with different resolutions, evolve in this model with adaptation. Adaptive capabilities enable effective domain decomposition in the evolving problem with damage, keeping a balance between computational efficiency and accuracy. Macroscopic analysis is done with the CDM model of Raghavan and Ghosh (2005) for high efficiency. Pure micromechanical analysis is computationally exhaustive and the adaptive methodology optimally reduces this region to a minimum. The Voronoi cell finite element model (Ghosh et al., 2000; Li and Ghosh, 2004) is effectively utilized for efficient micromechanical analysis of extended microstructural regions. The numerical examples establish the accuracy and efficiency aspects of the model, as well as demonstrate its capability in handling problems involving damage in large composite domains. Overall this work lays an effective foundation for

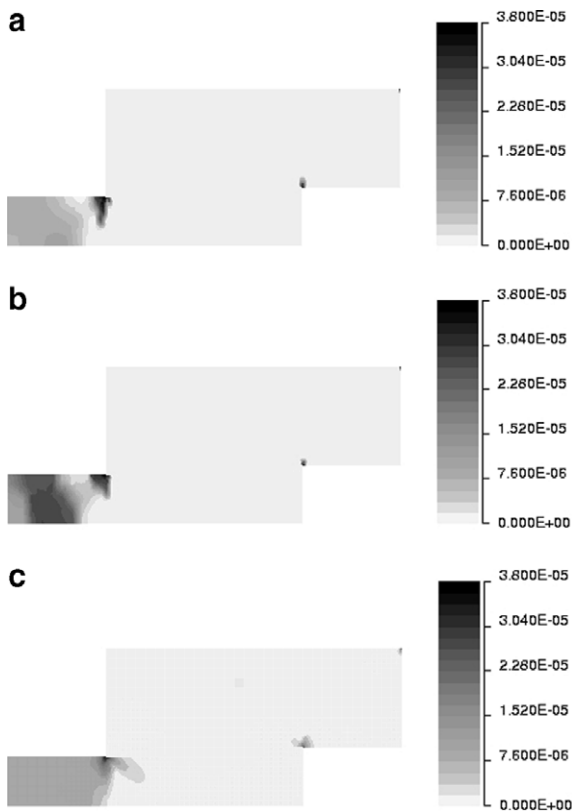


Fig. 20. Distribution of  $W_d$  with  $V_f = 40\%$  and different cohesive parameters: (a) case C1, (b) case C2, and (c) case C3, at the end of loading.

solving multi-scale problems involving localization, damage and crack evolution that may be impossible to achieve using any single scale model.

### Acknowledgements

This work has been supported by the Air Force Office of Scientific Research through Grant No. F49620-98-1-01-93 (Program Director: Dr. B. L. Lee) and by the Army Research Office through Grant No. DAAD19-02-1-0428 (Program Director: Dr. B. Lamattina). This sponsorship is gratefully acknowledged. Computer support by the Ohio Supercomputer Center through Grant #PAS813-2 is also gratefully acknowledged.

### References

- Bulsara, V.N., Talreja, R., Qu, J., 1999. Damage initiation under transverse loading of unidirectional composites with arbitrarily distributed fibers. *Comput. Sci. Technol.* 59, 673–682.
- Carol, I., Rizzi, E., Willam, K., 1994. A unified theory of elastic degradation and damage based on a loading surface. *Int. J. Solids Struct.* 31 (20), 2835–2865.
- Chow, C.L., Wang, J., 1987. An anisotropic theory of elasticity for continuum damage mechanics. *Int. J. Fracture* 20, 381–390.
- Cordebois, J.P., Sidoroff, F., 1982. Anisotropic damage in elasticity and plasticity. *J. Mech. Theor. Appl.*, 45–60.
- Fish, J., Shek, K., 2000. Multiscale analysis of composite materials and structures. *Comput. Sci. Technol.* 60, 2547–2556.
- Fish, J., Yu, Q., Shek, K., 1999. Computational damage mechanics for composite materials based on mathematical homogenization. *Int. J. Numer. Meth. Eng.* 45, 1657–1679.
- Ghosh, S., Moorthy, S., 1998. Particle cracking simulation in non-uniform microstructures of metal–matrix composites. *Acta Metall. Mater.* 46 (3), 965–982.
- Ghosh, S., Lee, K., Moorthy, S., 1995. Multiple scale analysis of heterogeneous elastic structures using homogenization theory and Voronoi cell finite element method. *Int. J. Solids Struct.* 32 (1), 27–62.
- Ghosh, S., Nowak, Z., Lee, K., 1997. Quantitative characterization and modeling of composite microstructures by Voronoi cells. *Acta Mater.* 45, 2215–2234.
- Ghosh, S., Ling, Y., Majumdar, B., Kim, R., 2000. Interfacial debonding analysis in multiple fiber reinforced composites. *Mech. Mater.* 32, 561–591.
- Ghosh, S., Lee, K., Raghavan, P., 2001. A multi-level computational model for multi-scale damage analysis in composite and porous materials. *Int. J. Solids Struct.* 38 (14), 2335–2385.
- Kachanov, L.M., 1987. *Introduction to Continuum Damage Mechanics*. M. Nijhoff, Dordrecht, Boston.
- Lee, K., Ghosh, S., 1999. A microstructure based numerical method for constitutive modeling of composite and porous materials. *Mater. Sci. Eng. A* 272, 120–133.
- Li, S., Ghosh, S., 2004. Debonding in composite microstructures with morphological variations. *Int. J. Comput. Meth.* 1 (1), 121–149.
- Li, S., Ghosh, S., 2006. Extended Voronoi cell finite element model for multiple cohesive crack propagation in brittle materials. *Int. J. Numer. Meth. Eng.* 65, 1028–1067.
- Moorthy, S., Ghosh, S., 2000. Adaptivity and convergence in the Voronoi cell finite element model for analyzing heterogeneous materials. *Comput. Meth. Appl. Mech. Eng.* 185, 37–74.
- Oden, J.T., Zohdi, T.I., 1997. Analysis and adaptive modeling of highly heterogeneous elastic structures. *Comput. Meth. Appl. Mech. Eng.* 148, 367–391.
- Ortiz, M., Pandolfi, 1999. A finite-deformation irreversible cohesive element for three-dimensional crack-propagation analysis. *Int. J. Numer. Meth. Eng.* 44, 1267–1282.
- Pyrz, R., 1994. Quantitative description of the microstructure of composites. Part I, Morphology of unidirectional composite systems. *Comput. Sci. Technol.* 50, 197–208.
- Raghavan, P., Ghosh, S., 2004a. Concurrent multi-scale analysis of elastic composites by a multi-level computational model. *Comput. Meth. Appl. Mech. Eng.* 193 (6-8), 497–538.
- Raghavan, P., Ghosh, S., 2004b. Adaptive multi-scale computational modeling of composite materials. *Comput. Model. Eng. Sci.* 5 (2), 151–170.
- Raghavan, P., Ghosh, S., 2005. A continuum damage mechanics model for unidirectional composites undergoing interfacial debonding. *Mech. Mater.* 37 (9), 955–979.
- Shan, Z., Gokhale, A.M., 2002. Representative volume element for non-uniform micro-structure. *Comput. Mater. Sci.* 24, 361–379.
- Smit, R.J.M., Brekelmans, W.A.M., Meijer, H.E.H., 1998. Prediction of the mechanical behavior of nonlinear heterogeneous systems by multi-level finite element modeling. *Comput. Meth. Appl. Mech. Eng.* 155 (1-2), 181–192.
- Swaminathan, S., Ghosh, S., Pagano, N.J., 2006a. Statistically equivalent representative volume elements for composite microstructures, Part I: Without damage. *J. Comput. Mater.* 40 (7), 583–604.
- Swaminathan, S., Ghosh, S., Pagano, N.J., 2006b. Statistically equivalent representative volume elements for composite microstructures, Part II: With evolving damage. *J. Comput. Mater.* 40 (7), 605–621.
- Tamma, K.K., Chung, P.W., 1999. Woven fabric composites: developments in engineering bounds, homogenization and applications. *Int. J. Numer. Meth. Eng.* 45, 1757–1790.
- Terada, K., Kikuchi, N., 2000. Simulation of the multi-scale convergence in computational homogenization approaches. *Int. J. Solids Struct.* 37, 2285–2311.
- Vemaganti, K., Oden, J.T., 2001. Estimation of local modeling error and goal-oriented adaptive modeling of heterogeneous materials, Part II: a computational environment for adaptive modeling of heterogeneous elastic solids. *Comput. Meth. Appl. Mech. Eng.* 190, 6029–6214.
- Zhu, Y.Y., Cescotto, S., 1995. A fully coupled elasto-visco-plastic damage theory for anisotropic materials. *Int. J. Solids Struct.* 32 (11), 1607–1641.
- Zienkiewicz, O.C., Zhu, J.Z., 1992. The superconvergence patch recovery and a posteriori error estimates. Part I: The recovery technique. *Int. J. Numer. Meth. Eng.* 33, 1331–1364.
- Zohdi, T.I., Wriggers, P., 1999. A domain decomposition method for bodies with heterogeneous microstructure based on material regularization. *Int. J. Solids Struct.* 36, 2507–2525.